The Effect of Non-solvent Post-Processing Induced Structural and Morphological Changes on the Optoelectronic Properties of $CsPbBr_3$ Nanocrystals

Bapi Pradhan[a],‡, Irina Skvortsova[a,b],‡, Sumea Klokic[c], Amitrajit Mukherjee[a], Alexis Villanueva-Antolí[d], Jonathan Vandenwijngaerden[a], Peiran Wang[a], Jhonatan Rodriguez-Pereira[e,f], Ignacio Utreras-Asenjo[g], Andrés F. Gualdrón-Reyes[d,g], Thomas J. N. Hooper[h], Dimitrios Sakellariou[h], Michael Paulus[i], Christian Sternemann[i], Heinz Amenitsch[c], Iván Mora-Seró[d], Elke Debroye[a], Sara Bals[b], Eduard Fron[a,]* and Johan Hofkens[a,]**

[a]Department of Chemistry, KU Leuven, Celestijnenlaan 200F, 3001 Heverlee, Belgium.

[b]Electron Microscopy for Materials Research and NanoLight Centre of Excellence, University of Antwerp, Groenenborgerlaan 171, 2020 Antwerp, Belgium.

[c]Institute of Inorganic Chemistry, Graz University of Technology, Stremayrgasse 9/IV, Graz 8010, Austria.

[d]Institute of Advanced Materials (INAM), Universitat Jaume I, Castelló de la Plana, Castellón 12071, Spain.

[e]Center of Materials and Nanotechnologies, Faculty of Chemical Technology, University of Pardubice, Nam. Cs. Legii 565, Pardubice, 53002 Czech Republic.

[f]Central European Institute of Technology, Brno University of Technology, Purkynova 123, Brno, 61200 Czech Republic.

[g]Facultad de Ciencias, Instituto de Ciencias Químicas, Universidad Austral de Chile, Isla Teja, Valdivia, 5090000 Chile.

[h]Centre for Membrane Separations, Adsorption, Catalysis and Spectroscopy for Sustainable Solutions (cMACS), KU Leuven, Leuven 3001, Belgium.

[i]Fakultät Physik/DELTA, Technische Universität Dortmund, 44221 Dortmund, Germany.

KEYWORDS. $CsPbBr_3$ nanocrystals • STEM imaging • In-situ SAXS • Time-resolved spectroscopy • LEDs

ABSTRACT. Significant efforts have been devoted to optimizing the post-synthesis processing of all-inorganic colloidal $CsPbBr_3$ nanocrystals (NCs) to achieve stable and ultrapure green emission. However, these NCs harbor a variety of compositional, structural, and surface defects, which undergo dynamic changes during non-solvent purification. Despite recent advances, the mechanisms underlying degradation during purification and their effects on the photophysical properties of $CsPbBr_3$ NCs remain unclear. In this study, we examine how the polarity of non-solvents influences the structural integrity, packing behavior, defects formation, as well as optical properties of the resultant NCs, *i.e.* photoluminescence (PL) blinking, and charge-carrier recombination dynamics. Using synchrotron-based *in situ* small-angle X-ray scattering, we show that ligand-shell removal during purification induces NC aggregation through a hierarchical, turbostratically stacked assembly process. *Ex situ* grazing-incidence X-ray scattering further reveals the atomic and nanoscale orientational ordering in NC thin films. Transmission electron microscopy demonstrates that ketone-based washing results in rapid, disordered aggregation and planar defect formation, whereas ester-based washing leads to slower aggregation without stacking faults. Moreover, single-particle PL microscopy indicates pronounced blinking in ketone-treated NCs, attributed to nonradiative structural defect formation. Finally, our findings suggest that ketone-processed NCs exhibit poor electroluminescence performance, whereas ester-processed NCs retain structural integrity and achieve external quantum efficiencies of up to ~17.6% in LEDs.

INTRODUCTION.

$CsPbBr_3$ nanocrystals (NCs) are excellent optoelectronic materials due to their intrinsic defect tolerance nature, robust structural stability, and bright photoluminescence, as demonstrated in various bottom-up fabricated optoelectronic devices, including LEDs[1], solar cells[2], photodetectors[3], lasers[4], electronic displays[5,6], scintillators[7], and photocatalysts[8,9]. The surface of colloidal $CsPbBr_3$ NCs is typically stabilized by amphiphilic long-chain surfactants. The most common surfactants are a binary mixture of oleic acid (OA) and oleylamine (OLA) that enable stable colloidal dispersions in low-polarity solvents such as hexane (dielectric constant ε = 1.88 at 25 °C) or toluene (ε = 2.38).[10] The NC surfaces are predominantly terminated by oleylammonium bromide or Cs-oleate species, where a dynamic equilibrium exists between bound and unbound ligand states.[11] The combination of dynamic ligand binding and the soft ionic nature of $CsPbBr_3$ NCs makes the non-solvent purification process particularly delicate, with only a narrow time window allowing for effective purification without structural degradation. Both the polarity and relative volume of the non-solvent play a key role in determining colloidal stability by regulating the removal of excess unbound ligands, unreacted precursors, and by-products. Purification is critical for the integration of NCs into optoelectronic devices, as a high density of surface ligands and excess organics typically impedes charge injection into the NCs by acting as an insulating barrier.[1,12] Reducing ligand concentration promote efficient charge injection in devices, which in turn minimizes Joule heating.[13] This reduction is beneficial for enhancing thermal stability and improving overall conductivity. Higher conductivity reduces local carrier accumulation, thereby suppressing Auger recombination processes.[14,15] However, an insufficient number of surface ligands can lead to undesirable NC aggregation and increased size dispersity.[16] This results in PL quenching, spectral peak shifts, and broadening of the full width at half maximum (FWHM).[17]

Furthermore, the addition of polar non-solvents must be performed rapidly to minimize the interaction between the ionic surface of the NCs and the polar functional groups of the non-solvent.[18] This step induces flocculation and aggregation of the lyophobic, ligand-capped NCs, governed by the free energy

of interpenetration, while excess surfactants are displaced into the supernatant.[19] In some studies, the purification step has been entirely omitted to prevent NC degradation.[7,11,20–24] Repeated washing cycles are known to degrade the optical properties of $CsPbBr_3$ NCs.[17] Notably, purification using highly polar solvents such as dimethylformamide (DMF) leads to a complete morphological transformation from nanocubes to nanodots.[25] These observations highlight the complexity of purifying $CsPbBr_3$ NCs, given their high ionic character and dynamically bound surface ligands. Carefully designed purification strategies are therefore essential to retain and optimize their optoelectronic properties. Despite growing interest, the underlying fundamental processes and related structural transformations that occur during NC purification remain poorly understood and warrant a systematic investigation.

Unfortunately, purification processes applied to perovskite NCs to remove excess ligands often lead to the formation of surface defects.[26] In the case of mixed-halide $CsPb(I/Br)_3$ NCs, it has been shown that iodide ions are preferentially removed during purification, while bromide ions tend to retain.[27,28] Moreover, solvent polarity plays a critical role in determining NC stability and performance. Based on device performances, it has been suggested that washing with high-dielectric-constant solvents, such as 1-butanol ($\varepsilon = 17.1$), should be avoided due to their detrimental impact on NC integrity and performance.[29] Despite these observations, the underlying mechanisms via which polar non-solvents negatively influence the optoelectronic properties, particularly for $CsPbBr_3$ NCs, remain poorly understood.[30] Gaining insight into these effects is essential for advancing the practical use of $CsPbBr_3$ NCs in photonic and optoelectronic applications.

Herein, we investigate the interplay between two commonly used non-solvents, one ketone and one ester, with markedly different polarities: acetone[18] (Ac, polarity index $p = 5.1$, dielectric constant $\varepsilon = 20.7$) and ethyl acetate[1] (Et, $p = 4.4$, $\varepsilon = 6.02$). We examine how these post-synthesis purification treatments affect the ligand shell, surface chemistry, structural integrity, optical and photophysical properties, and device performance of $CsPbBr_3$ NCs. Steady-state optical measurements reveal nearly identical optical

properties for pristine and post-processed NCs. However, transmission electron microscopy (TEM) shows clear differences in the structure, with prominent Ruddlesden-Popper (RP) planar defects observed in acetone-treated samples. Synchrotron-based in situ small-angle X-ray scattering (SAXS), captures the real-time removal of surface ligands from $CsPbBr_3$ NCs upon exposure to the non-solvent. Complementary analyses using proton nuclear magnetic resonance (^{1}H NMR) and X-ray photoelectron spectroscopy (XPS) provide further insight into the surface ligand removal mechanisms and chemical composition. Time-resolved spectroscopy reveals that exciton formation and relaxation occur on a femtosecond to picosecond timescale, while their lifetimes extend to the nanosecond range. Measurements in the nanosecond timescale also detect photogenerated free carriers and provide insights into their recombination behavior. To correlate the defect formation, we examined single-particle PL blinking in pristine and processed $CsPbBr_3$ NCs. Acetone-treated NCs exhibit frequent blinking and photobleaching, particularly under high excitation, indicating increased defect density. In contrast, Et-treated and pristine NCs show suppressed blinking and improved photostability. These observations suggest that highly polar solvents promote defect formation by stripping surface ligands. A proof-of-concept LED device demonstrates a 500-fold increase in luminescence and an external quantum efficiency (EQE) of approximately 17.6 percent for Et-treated NCs, compared to about 8 percent for those treated with Ac. Overall, this study provides valuable insight into post-synthesis transformations during purification and highlights the importance of defect control for the development of high-performance photonic devices.

RESULTS AND DISCUSSION.

$CsPbBr_3$ NCs were synthesized following established protocols by injecting cesium-oleate to a mixture of Pb-oleate and oleylammonium bromide at 190 °C.[15,20,31,32] The reaction was quenched approximately 10 seconds after Cs-oleate injection to prevent further growth into the bulk phase.[20,33] The resulting colloid was centrifuged and redispersed in hexane, and this dispersion is referred to as the starting colloid

(hereafter termed CPB), see Supporting Information (SI) for further details. To evaluate the influence of non-solvents on the purification process, CPB dispersions (10 μM in hexane) were treated with Ac and Et at volume ratios of 1:1 and 1:2 (non-solvent:CPB), denoted as Ac1/Et1 and Ac2/Et2, respectively

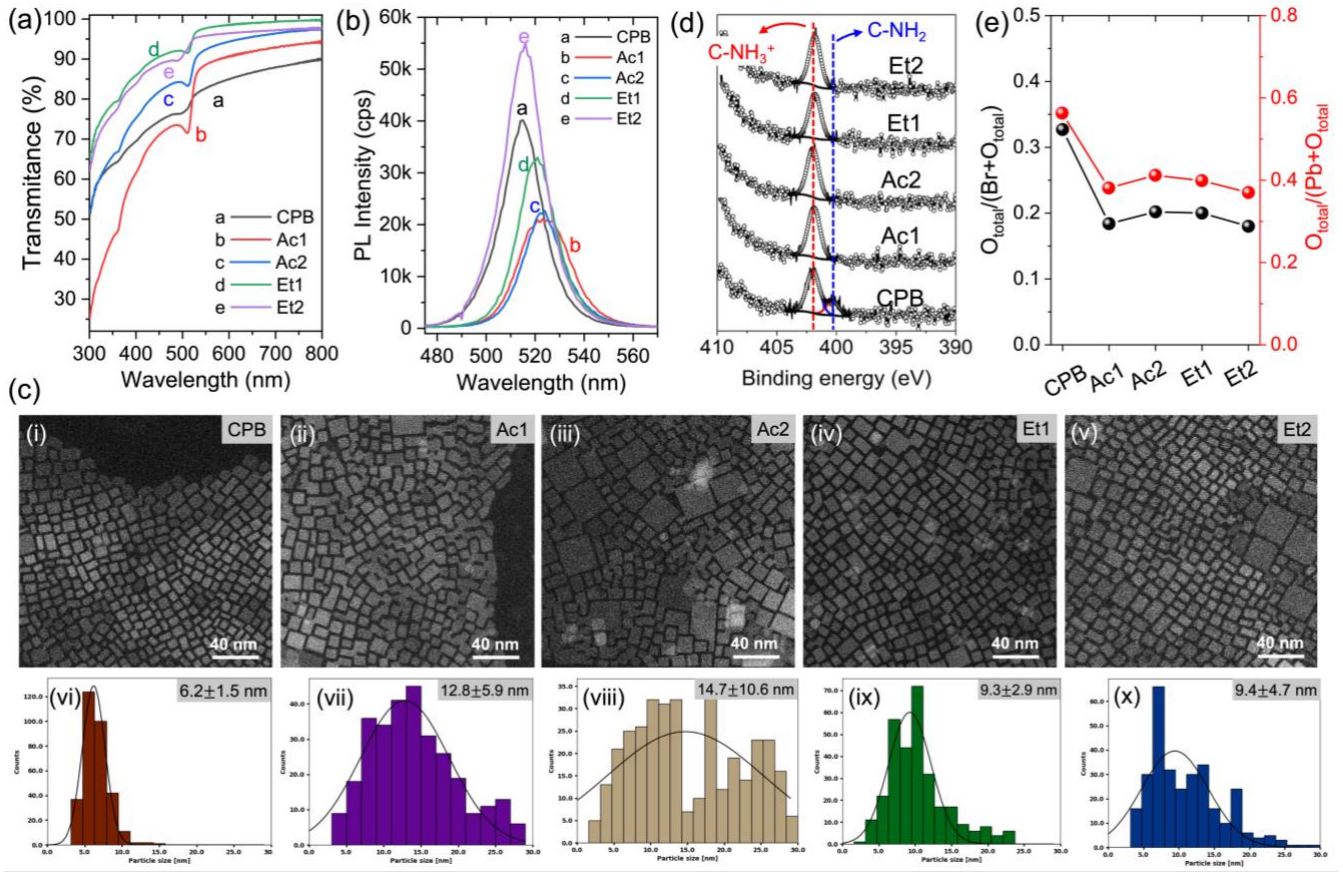


Figure 1. Steady-state optical properties, morphology and surface ligand binding of $CsPbBr_3$ NCs following various post-synthesis purification stages. Room-temperature (a) *UV-Vis* optical transmittance and (b) PL spectra of CPB, Ac1, Ac2, Et1 and Et2 NC thin films. Where CPB is pristine starting colloid in hexane, Ac1/Et1 and Ac2/Et2 are isolated NCs using 1:1 and 1:2 volume ratios of Ac and Et. (C) HAADF-STEM overview images (i-v) and corresponding particle size distributions (vi-x) for CPB, Ac1, Ac2, Et1 and Et2 NCs. (d) HR-XPS N 1s spectra shows the surface chemical state variation of the CPB, Ac1, Ac2, Et1 and Et2 NCs, associated with C-NH_2 (400 eV) and C-NH_3^+ (402 eV) moieties from OLA and oleylammonium cations. (e) The extent of surface ligand removal from the variation in oxygen-to-bromine and total oxygen-to-lead ratios of different $CsPbBr_3$ NCs.

(see Experimental Section, SI). Zeta potential measurements for all samples revealed similar negative values (~-32 mV), indicating retained colloidal stability after non-solvent treatment.[34] Purification using acetone is known to remove excess carboxylate anions in the form of ligand-ion pairs from crude dispersions without proton transfer steps.[18,27,35–39] In contrast, purification with Et tends to exchange surface oleate anions with acetate via a proton transfer mechanism.[1,40–43] Steady-state UV-Vis absorption and PL spectroscopy of NC thin films show similar spectral features across samples (Fig. 1a,b), with only minor shifts in absorption and emission maxima (within ±10 nm). Comparable results were obtained in solution-phase measurements, where no significant bandgap changes were observed (Fig. S1a and Table S1-2). All samples displayed bright, relatively narrow emissions centered around 515-522 nm, characteristic of excitonic recombination from the lowest excitonic state.[44] This exciton state involves a hole in the s-type valence band Coulombically bound to an electron in the p-type Pb orbital.[45] The PL quantum yield (PLQY) ranged from ~16% to 67% in both solution and thin-film forms (Table S3, SI).[11,22]

The morphology of the $CsPbBr_3$ NCs was examined using high-angle annular dark-field scanning transmission electron microscopy (HAADF-STEM). HAADF-STEM images (Fig. 1c, i-v) reveal that all samples include square and rectangular NCs, with size distributions varying depending on the polarity and volume of the non-solvent used during purification. In particular, Ac-treated samples (Ac1 and Ac2) exhibit broader size distributions with additional populations of larger NCs, as shown in the histograms (Fig. 1c ii, iii, vii, viii). Notably, increasing the Ac volume during purification (Ac2) results in an almost bimodal size distribution, with a secondary size population centred around ~24-25 nm (Fig. 1c iii, viii). A similar trend is observed in Et-treated samples, but the extent of size broadening is considerably reduced (Fig. 1c v, x). Specifically, for Et2 NCs, a significant number of particles fall within the 5-7 nm size range, which correlates with the observed blue shift in both absorption and emission spectra (Fig. 1a,b) relative to Ac1 and Ac2. These findings suggest different underlying purification mechanisms driven by the polarity of the non-solvent. Dynamic light scattering (DLS) measurements further support the observed trends in size evolution (Fig. S1b). Since it was previously observed that for mixed-halide $CsPb(Br/I)_3$

NCs, Ac purification step causes prominent halides etching,[27] the average elemental composition of the Ac1 and Et1 NCs was mapped using energy-dispersive X-ray spectroscopy (EDS) (Fig. S2), however, no significant differences in elemental composition were observed between the Ac- and Et-washed samples.

During the optimization of high-resolution (HR) STEM imaging conditions, a clear difference in surface sensitivity to the electron beam was observed between Ac- and Et-treated NCs.[46] Ac-processed NCs were more susceptible to electron beam-induced degradation under the same electron dose compared to those treated with Et (Fig. S3). This variation in surface stability suggests that the extent of removal of stabilizing ligands such as OA and OLA differs between the two post-processing methods. As a result, imaging of the Ac1 sample was performed at a lower electron dose (<800 $e^-/Å^2$), whereas the Et1 sample could tolerate a higher dose (>1000 $e^-/Å^2$). Fast Fourier Transform (FFT) patterns for the acquired HRSTEM images showed that both Ac1 and Et1 NCs might contain not only the orthorhombic crystal phase but also a cubic one (Fig. S4). The phase might be dependent on NC size, which has been previously reported for $CsPbBr_3$ NCs.[47] On the other hand, the absence of additional reflections in FFT patterns for small $CsPbBr_3$ NCs (Fig. S4b,f) can be attributed to the inherently weak signal of orthorhombic features, which becomes too faint to detect as the particle size decreases, leading to an apparently cubic FFT pattern.

To further investigate the crystal structure of the pristine and post-processed NCs, solution-phase wide-angle X-ray scattering (WAXS) was performed. The obtained high-resolution diffraction patterns reveal a dominant orthorhombic phase (*Pnma*) for all $CsPbBr_3$ NCs (Fig. 2a).[48] While contributions from the cubic phase cannot be entirely excluded, they are difficult to distinguish due to peak broadening and size inhomogeneity.[47,49] Surface ligand coverage for CPB, Ac2, and Et2 shows a similar trend at $q \approx 14$ nm^{-1}, whereas Ac1 and Et1 exhibit ligand restructuring around $q \approx 5$ nm^{-1} (Fig. 2a), however, background solvent scattering subtraction cannot be completely normalized.[50] The optoelectronic performance of bottom-up fabricated NC thin-film devices strongly depends on crystallinity and nanoscale ordering,

which in turn are influenced by particle monodispersity and deposition conditions.[51,52] To assess the impact of non-solvent treatment on crystalline structure and orientational ordering, grazing-incidence wide-angle X-ray scattering (GIWAXS) and grazing-incidence small-angle X-ray scattering (GISAXS) measurements were conducted (Fig. 2). All NC films display distinct atomic-scale ordering, as evident from the sharp diffraction spots in the 2D GIWAXS patterns (Fig. 2b-d and Fig. S5). Radial cuts along in-plane, out-of-plane, and total directions were analyzed (Fig. S5), revealing improved crystallinity from CPB to Ac and Et samples, attributed to the increase in particle size (Fig 1c). The extent of orientational ordering varies across samples, with out-of-plane ordering generally stronger than in-plane. Grain orientation was further quantified by extracting the azimuthal intensity profile (χ-plot) from the Debye-Scherrer rings of the GIWAXS data at the <121> , <200>, <002> planes at 15 nm^{-1} ($\chi = -80°$ to $+80°$, where $\chi = 0°$ corresponds to out-of-plane and $\chi = \pm 90°$ to in-plane) (Fig. 2e). FWHM analysis of the azimuthal peaks, fitted with a Pearson VII function, indicates a trend in crystallographic domain alignment: CPB >> Et1 > Ac1. This suggests that non-solvent-induced NC coarsening significantly influences structural order and macroscopic behavior. To probe nanoscale ordering, GISAXS measurements were performed in the q range of −1 to +1 nm^{-1} (Fig. 2f-i). The strongest lateral ordering was observed only for CPB along the horizontal axis (Fig. 2f) at ~0.53 nm^{-1}, from which the interparticle distance of the particles can be calculated to be ~11.2 nm (Fig. 2i). One-dimensional line cuts show a complete reduction in nanoscale ordering for Ac and Et samples (Fig. 2i). A more detailed analysis, including incident angle-dependent GISAXS, would be required to fully resolve nanoscale structural features which is beyond the scope of this study.

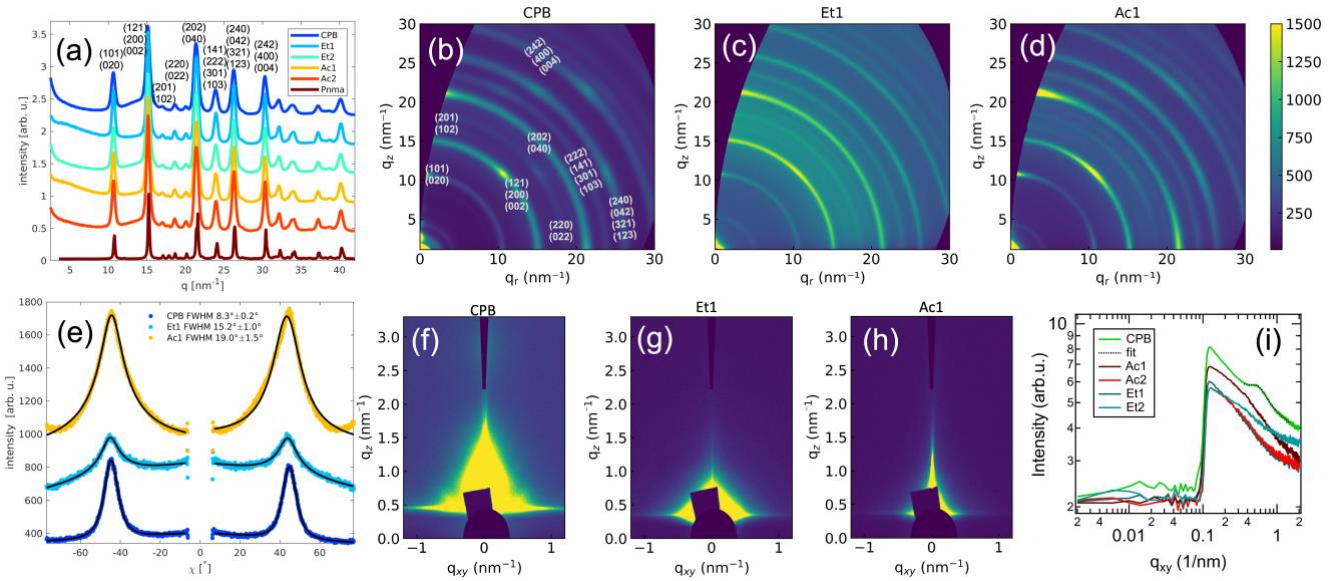


Figure 2: (a) Solution phase transmission WAXS of $CsPbBr_3$ NCs after background subtraction of the diffraction contribution from the liquid hexane phase indexed with the *Pnma* orthorhombic structure. (b-d) 2D GIWAXS images of CPB, Ac1, and Et1 NC thin-films (e) Chi-plot of the orientational ordering of CPB, Ac1, Et1 thin-films using the Bragg reflection corresponding to (121), (200), (002) planes. Inset shows the FWHM values. (f-h) 2D GISAXS images of CPB, Ac1, and Et1 NC thin-films. (i) Horizontal line cuts of the 2D GISAXS data for CPB taken at the Yoneda region and the corresponding fit (see SI for details on the fitting function).

To elucidate the surface chemistry and average composition of $CsPbBr_3$ NCs after purification with different acetone Ac and Et volume ratios, XPS was performed. Survey spectra confirm the presence of C, N, O, Cs, Pb, and Br (Fig. S6), with quantitative data summarized in Table S4 (SI). High-resolution (HR) XPS Cs 3d spectra display the characteristic $3d_{5/2}/3d_{3/2}$ doublet at 725/739 eV (Fig. S7a), confirming Cs^+ in the perovskite lattice.[53] The Br 3d doublet at 68/69 eV (Fig. S7b) corresponds to Br^- from $[PbBr_6]^{4-}$ octahedra, and the Pb 4f doublet at 138/143 eV (Fig. S7c) is attributed to Pb^{2+}.[54] The N 1s spectrum of CPB reveals peaks at 400 and 402 eV, assigned to C-NH_2 (OLA) and C-NH_3^+ (oleylammonium), respectively (Fig. 1d). After purification, only the C-NH_3^+ signal remains, indicating selective removal of oleylamine.[55] The O 1s spectra show contributions from Pb-O (~530 eV), O=C-O (~531 eV), and C-

O (~532 eV) bonds, reflecting the presence of carboxylate ligands.[56] Quantitative analysis reveals reduced Cs^+ content in Ac-treated NCs compared to Et-treated ones, suggesting more Cs^+ surface vacancies in the presence of acetone (Table S4). This may explain the increased C-NH_3^+ fraction observed for Ac1 and Ac2, as OLA^+ species likely compensate for Cs^+ deficiencies.[21] Both non-solvents reduce O=C–O signal intensity, indicating detachment of native oleate ligands, with Et2 showing the most pronounced effect. Notably, Et1-treated NCs exhibit a higher Pb-O signal compared to Ac1 and Ac2 (Fig. S7d), likely due to ligand exchange with acetate rather than simple oleate removal.

Alkyl acetates, such as methyl acetate, are known to replace oleate species on the perovskite surface, enhancing carrier transport and promoting defect passivation.[40–43] Although Et1 and Et2 NCs show similar overall compositions, Et2 exhibits a higher carbon content (Table S4), likely due to the larger volume of Et used during washing. This increased carbon presence may explain the absence of detectable Pb-O bonds in Et2. Acetate species likely interact with the NC surface, compensating halide vacancies and suppressing Pb-O coordination observed in Et1. This suggests Pb-O bonds also form during ligand exchange in Et2 but are not detected due to better compensation. Notably, the total oxygen to bromine and oxygen to lead ratios, $[(O_{total}/Br+O_{total})]$ and $[(O_{total}/Pb+O_{total})]$, are higher and lower for Et1, respectively, compared to Ac1 and Ac2 (Fig. 1e and Fig. S6d). Despite this, Et1-treated NCs have fewer point defects than Ac-treated ones, considering the Cs deficiency and elevated OLA^+ fraction in Ac samples. Et2 shows the lowest oxygen ratios, indicating that excess Et further reduces defect density. The lower oxygen content introduced by Et implies fewer halide vacancies are formed and thus fewer need to be compensated. Overall, ethyl acetate post-treatment, particularly at higher volumes, yields a less defective perovskite, as evidenced by near-stoichiometric Cs/Pb ratios (~1.0; Table S4) and reduced surface degradation.

To gain further insight into the surface chemistry of washed and unwashed $CsPbBr_3$ NCs, proton (^1H) NMR spectroscopy was performed. The ^1H NMR spectra of NCs dispersed in deuterated cyclohexane

(C_6D_{12}) are shown in Fig. S8. Signals at δ = 5.64 and 4.83 ppm correspond to residual 1 octadecene (1 ODE), used as the synthesis solvent. The peak at δ = 6.45 ppm and the shoulder at δ = 3.51 ppm (black spectrum) are assigned to protons of the ammonium group (NH_3^+) and the methylene group adjacent to NH_3^+ in oleylammonium (OLA^+) cations. The signal at δ = 2.10 ppm corresponds to the methylene group adjacent to the carboxyl moiety (COOH) of oleate (OA^-) species.[11,57,58] The resonance at δ = 5.25 to 5.22 ppm is attributed to vinylene protons in the hydrocarbon chains of OLA^+ and OA^-. Upon washing with Ac1, stronger signals from vinylene protons and CH_2 groups near COOH are observed compared to Et1 and Et2, indicating a higher presence of surface-bound OLA^+ and OA^-. As confirmed by XPS, acetone washing induces Cs^+ surface defects that are compensated by OLA^+ cations, resulting in an increased OLA^+ content. This suggests that free OA^- anions may interact with surface-bound OLA^+. In contrast, Et1 and Et2 treatment significantly reduces these NMR signals, consistent with the effective removal of OA^- from the NC surface.[59] These results confirm that washing with Et1 facilitates the removal of native surface ligands and partial replacement of OA^- with shorter chain acetate moieties, which may enhance electronic properties of the NCs for optoelectronic applications.

To elucidate the mechanism of surface ligand removal induced by non-solvent addition, we investigated the effect of the non-solvents on the NC purification process using *in-situ* synchrotron small-angle X-ray scattering (SAXS). A defined volume of non-solvent was introduced *via* a syringe pump into a dispersion of pristine CPB NCs (50 μM) in hexane, contained in a quartz capillary (Fig. 3a). Because of its higher density, the polar non-solvent diffuses downward, acting as an effective purifying agent. This diffusion created a concentration gradient along the vertical axis of the capillary, which was used to monitor the different stages of the NCs purification process. Following this, SAXS measurements were conducted at various vertical positions in a capillary (Fig. 3a and Table S5). The farthest point from the non-solvent front (position A) represents the unwashed NCs. The average NC size at this position was determined by 7.8 nm by fitting the respective SAXS pattern (Fig. S9a) and is in good agreement with TEM data (Fig. 1c).-Upon contact with acetone (Ac1, position B), a hierarchical self-assembly of $CsPbBr_3$ NCs into a

super-structure was observed (Fig. 3b,c). Increasing the volume of acetone (Ac2; CPB:Ac = 1:2) accelerated this superstructure formation process by approximately fivefold (Table S5 and Fig. S9b-d). This hierarchical self-assembly showed characteristic peaks in the respective SAXS pattern (Fig. 3b). Considering the relative peak positions with respect to q^*- (Fig. 3c), a two-dimensional nanoscale packing is observed from the scattering signal that is characterized by turbostratic stacking.[60,61] This hierarchical structure features regular interlayer spacing whereas in the in-plane direction, positional correlations between the layers lack any long-range order. This interpretation is further supported by the GIFT (General Indirect Fourier Transforamation) analysis of SAXS data into real space. The bead modelling of SAXS data generates the 3D structures of the pristine $CsPbBr_3$ NCs where an aspect ratio of 2.5:1 is obtained, implying nearly platelet structure (Fig. S10).[36]

This self-assembly process was previously proposed by Ye et al. and Sun et al., which is induced by the polar solvent causing a removal of OLA ligands on the PNC surface. This process then reduces the steric repulsion between the ligand-capped pristine $CsPbBr_3$ NCs by promoting a NC superstructure formation.[27,62] Typically, NCs dispersed in hexane remain stable because their surface ligands form a protective shell that screens attractive core interactions and introduces repulsive forces.[19,63] Steric repulsion varies with surface shape: flatter surfaces yield stronger repulsion due to denser ligand overlap, while highly curved surfaces of smaller NCs show weaker repulsion and are more prone to clustering.[19,63] Increasing the non-solvent concentration clearly removes the ligand shell, as evidenced by a shrinkage of the superstructure's d-spacing by Δd = 1.9 nm for both Ac1 and Et (position C, Fig. 3c). Given that the length of OLA is about 2.0 nm,[64] this confirms partial ligand shell removal caused by the polarity of Ac and Et (Fig. 3c, schematic on NCs present in position B and C). This is further supported by the appearance of a broad peak at $q \approx 2.2$ nm^{-1} (Fig. 3c), attributed to micellar OLA formation in solution, which is absent before NC washing (Fig. S9a).[65]

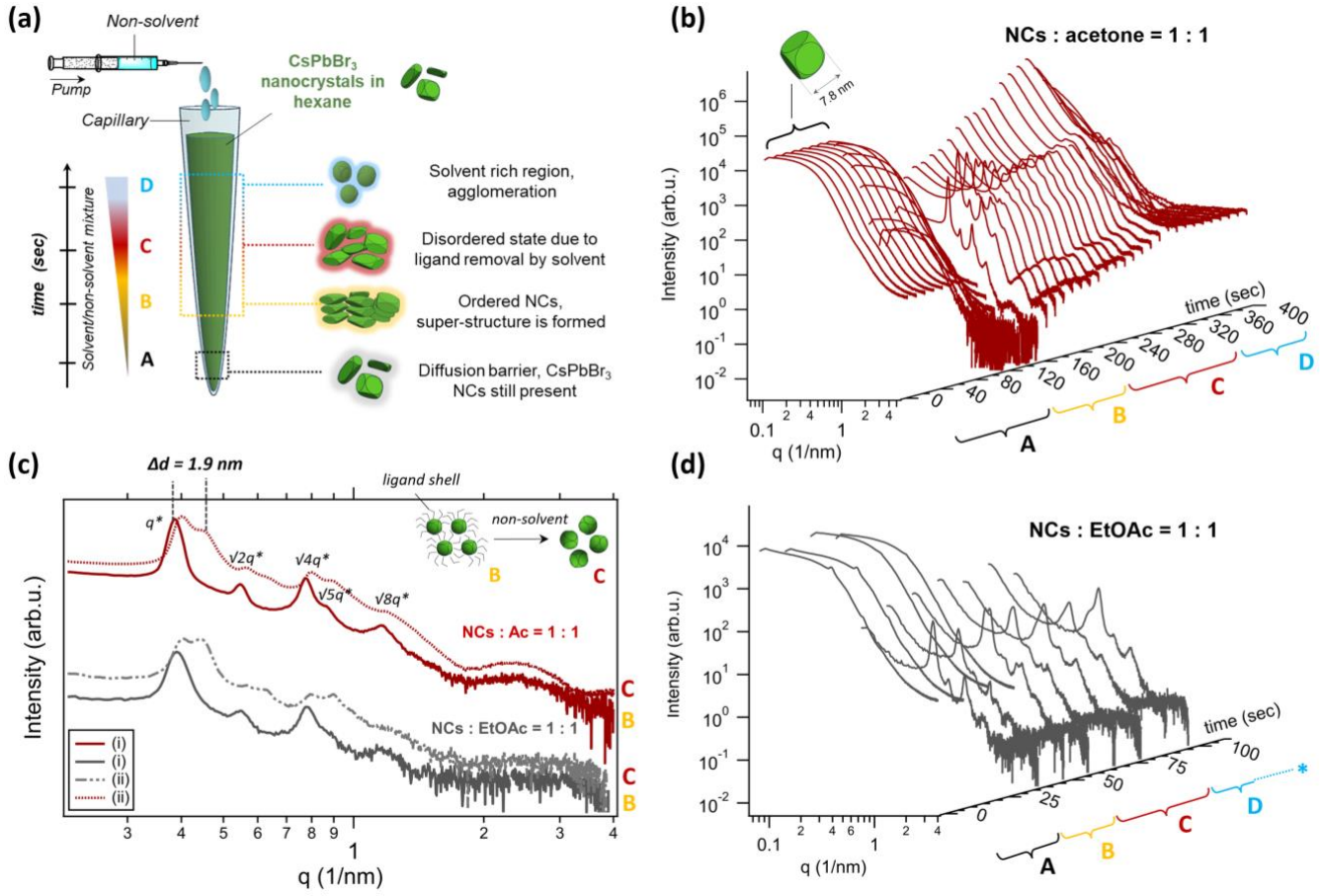


Figure 3. In-situ SAXS of non-solvent induced $CsPbBr_3$ NCs purification process. (a) Schematics of the NCs purification process monitored by *in-situ* SAXS. The diffusion of the polar non-solvent into the hexane dispersion of $CsPbBr_3$ NCs in capillary was vertically scanned at different spatial positions starting from the bottom of the capillary thus monitoring the influence of increasing solvent concentration on the NCs. The main processes are denoted with (A) presence of $CsPbBr_3$ NCs (no influence polar non-solvent), (B) formation of an ordered NC superstructure which at increasing solvent concentration leads (C) to a disordered state due to ligand removal, or (D) aggregation of particles. The evolution of the SAXS pattern over the course of the drop-wise non-solvent addition process is shown for Ac1 was monitored for CPB:Ac = 1:1 in (b) and for Et1 (CPB:Et = 1:1) in (d). The characteristic regions are labelled by *A-D*, where the color-coding is kept the same for all images. (c) Zoom-in on the SAXS patterns represent the ordered CPB superstructure formed upon initial contact with polar solvent (B, solid lines for Ac1 and Et), where a cubic and tetragonal stacking was deduced according to the ratio of the reflections with

respect to q^* = 0.38 nm^{-1}. The removal of the ligand shell is envisioned by a shrinkage of 1.9 nm in d-spacing due to extended polar solvent exposure in position C.

This further supports that upon contact with Ac, the OLA ligand shell is significantly removed, and free ligand molecules form micelles in solution. This process greatly reduces interparticle steric repulsion, allowing the formation of ordered assemblies. As ligand removal progresses, the NCs stack closer, evidenced by a Δq^* shift of 0.014 nm^{-1}, corresponding to a 0.5 nm reduction in the superstructure's d-spacing between states B and C (Fig. 3c and Table S6). SAXS data show that increasing Ac1 concentration drives the system to a fully disordered state, where in regions of high acetone concentration (position D), ordered $CsPbBr_3$ assemblies collapse into an aggregated phase (Fig. 3b), as the NC surface becomes fully exposed to the non-solvent (positions C-D, Fig. S9c,d). This agrees with HR-XPS results showing that Ac removes OLA^+ ligands more efficiently from the perovskite surface due to its higher dielectric constant and polarity (Table S4). Analysis of the scattering at the low-q range, which is particularly sensitive to the organization of superstructures, (fractal-) aggregates or fractal diffusion, shows pronounced changes in the power-law behavior expressed as q^{-D_f},[66] (where D_f is fractal dimensions) during NCs purification by Ac1 (Fig. S11). Unwashed NCs display a q^0 dependence (position A), typical for non-interacting globular particles, while initial exposure to Ac1 transitions through a q^{-2} behavior (position B), characteristic of two-dimensional NC nanoscale packing. With further exposure to Ac1, a q^{-4} scattering dependence (position C) is observed indicating that the assemblies evolve into a three-dimensional structure likely with sharp interfaces between solvent and solid particles[67], and upon prolonged treatment, a larger aggregate superstructure emerges, reflected by the decrease to q^{-2} and q^{-3} dependence, implying dense mass fractal clusters of particles (position D).[67] Exposure of NCs to Ac1 for over ~180 seconds causes complete structural degradation (position D, Fig. S9). An intrinsically Br-deficient structure, combined with high Cs dissolution and significant OLA release in acetone, acts as a catalyst for defect-rich, deteriorated nanostructures.[21,68]

In contrast, when using Et as the washing solvent, the transition to the disordered state occurs much more slowly (Fig. 3d), and NCs remain intact in the Et-rich region, unlike with Ac. Note that in Fig. 3d, only the scattering pattern from the first vertical scan at each capillary position is shown, while a total of 12 scans were performed to monitor the washing process over time (Fig. S9e and S12-13). Although ligand removal begins immediately upon sufficient contact with the polar non-solvent, comparing the q^* of the superstructure at position B and after Et exposure at position C (Fig. S12, SI) reveals a 2.1 nm reduction in *d*-spacing, indicating strong structural shrinkage after full ligand removal. This agrees with TEM results showing smaller particle size after Et1 washing compared to Ac1, which is further supported by optical absorption and photoluminescence data showing a blue shift consistent with reduced particle size (*vide supra*, Fig. 1a,b). The blue shift in absorption spectra has previously been linked to particle size reduction caused by washing with polar solvents.[27] After prolonged exposure to the polar solvent, the NCs maintain a remarkable degree of ordering in the Et-rich region D, indicating gentler ligand removal (Fig. S12d).[69] This is attributed to defect passivation by acetate anions, as shown by HR-XPS results, which protects the NC structure from immediate degradation. Gentler ligand removal is further supported by a less pronounced peak at $q = 2.2$ nm^{-1} that is attributed to free OLA. Therefore, washing NCs with Et does not lead to degradation, even during prolonged exposure, whereas Ac washing causes immediate degradation within minutes.

Based on STEM results and GIWAXS measurements, the crystal phase of all samples is expectedly the same. However, detailed HRSTEM analysis of Ac1 NCs revealed many crystals in which a sharp boundary separates the structure into two distinct regions (Fig. 4a and Fig. S14). Additionally, there is a half-unit offset of the crystal lattice in two perpendicular directions (Fig. 4a, yellow arrows). The resulting planar defect may act as a site for nonradiative recombination, which quenches the PL. From atomic column intensity maps[70] for this region (Fig. 4b), an abrupt intensity drop is observed in two lattice directions, indicating an immediate transition from Pb,Br-containing to Cs-containing atomic columns. Such defects are commonly known as Ruddlesden-Popper (RP) planar faults propagating through the

$CsPbBr_3$ NCs.[71–73] Theoretical calculations[72] predict the distance between CsBr layers (the "gap" size) to be approximately 3.70 Å, which matches perfectly with the ~3.66 Å distance measured from HAADF-STEM images (Fig. 4a). This confirms that the observed stacking faults (Fig. 4a) can be identified as [100]-oriented Ruddlesden-Popper defects. As discussed previously,[74–76] RP phase domains are often associated with doping of $CsPbX_3$ NCs; however, no dopants were introduced in this work. SAXS studies highlight the influence of solvent polarity on particle transition dynamics. Both acetone and ethyl acetate effectively remove the ligand shell from perovskite surfaces. However, due to its higher polarity, Ac leads to rapid ligand removal coupled with Cs dissolution, potentially causing planar defects that may arise from the agglomeration of neighboring NCs. Since as-synthesized $CsPbBr_3$ NCs tend to orient mostly in the same direction ($[100]_c$) with frequent surface termination with Cs+Br columns rather than Pb+Br columns, their agglomeration results in RP faults characterized by an additional CsBr layer between perovskite structures (Fig. 4c). To our knowledge, the impact of RP defects on the optical properties of metal halide perovskites has not yet been clearly explained. Therefore, we further investigate the optical properties (vide infra Fig. 4d-i and Fig. 5) to correlate the presence of RP planar defects and ligand removal/exchange with material performance.

Time-resolved spectroscopy elucidates the effect of the non-solvent on exciton recombination kinetics in the processed NCs both in solution and thin film. Exciton dynamics play a key role in the efficiency of luminescent devices, and a clear understanding of these processes is essential for device optimization. Using time-resolved spectroscopic techniques allows monitoring of exciton behavior over a wide range of energies and time scales. Time-Correlated Single Photon Counting (TC-SPC) performed on NCs on a picosecond to nanosecond time scale in solution and film revealed a multiexponential luminescence decay.[77] To assist with identifying the retrieved time components, we plotted their decay-associated spectra in Fig. 4d-g. In solution, the PL decays with rather similar time constants. Based on literature reports, we attribute the 1.6 ns and 6.1 ns components for Ac1, and the 2.2 ns and 6.3 ns components for Et1, to the decay of two single exciton species. Since multiple exciton formation can be ruled out under

400 nm excitation, these species likely correspond to two distinct crystal phases, as previously observed.[78,79] This interpretation aligns with earlier results showing the coexistence of cubic and orthorhombic phases arising from polydisperse size distribution. Interestingly, the large amplitude of the long-lived time constant suggests that excitons represent the main photogenerated species. Nevertheless, the components primarily contributing to the steady-state emission are the 17.9 ns and 19.6 ns lifetimes observed for Ac1 and Et1, respectively. Given that these time constants are significantly longer than typical excitonic lifetimes (1.7 to 7.0 ns),[80,81] and their spectral maxima are red-shifted (indicating lower transition energies), we assign these signals to the radiative recombination of photogenerated free carriers.[82] In combination with the moderate PLQYs, this suggests that a considerable fraction of the free carriers becomes trapped and undergoes non-radiative recombination. This finding stands in marked contrast to earlier reports, where PL was entirely attributed to exciton recombination.[78,79]

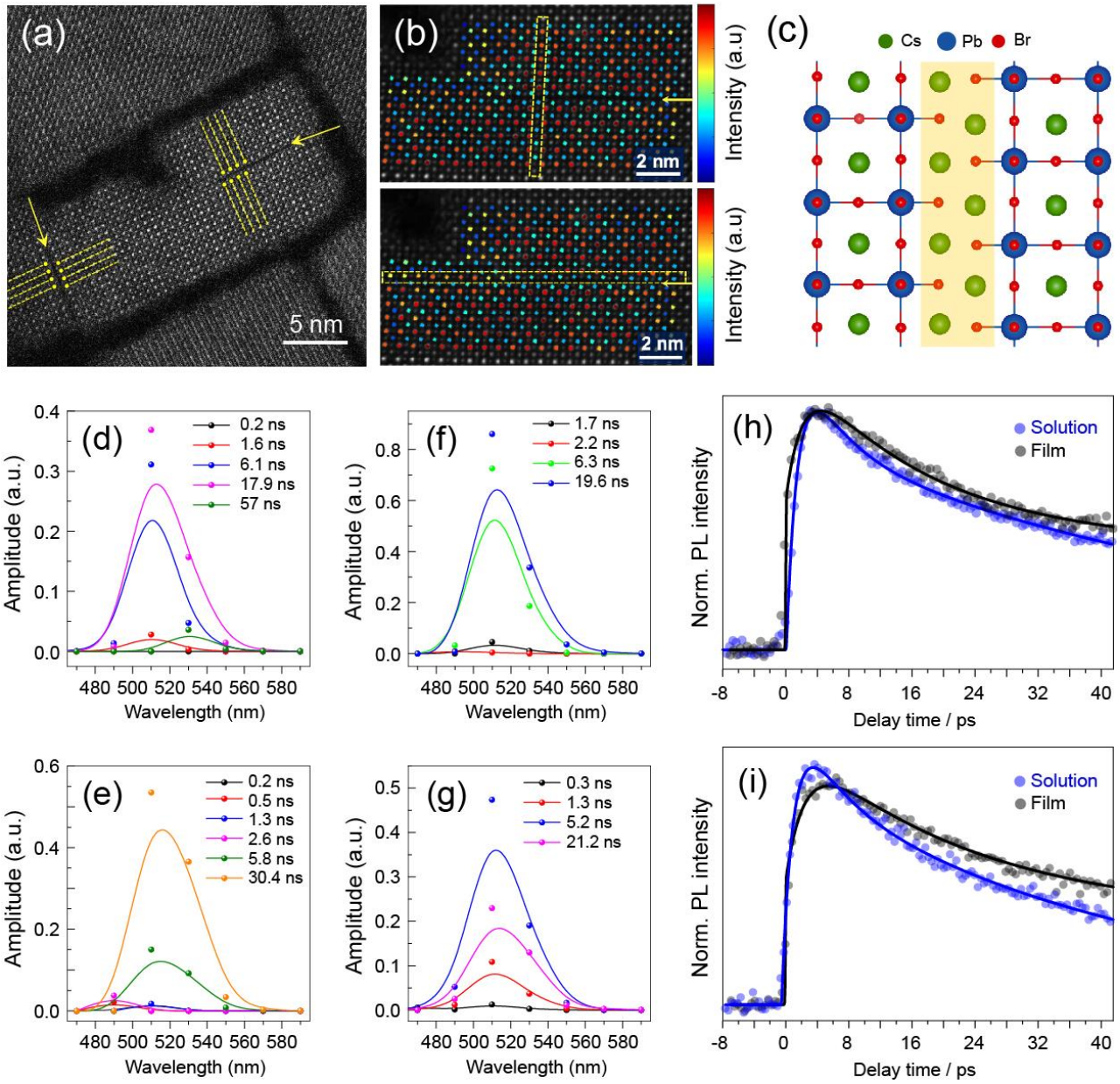


Figure 4. (a) High-resolution HAADF-STEM image showing the presence of RP planar defects for $CsPbBr_3$ Ac1 NCs. White dashed arrows highlight ½ lattice shifts. (b) This image is complemented with the atomic column intensity map. (c) A schematic model of RP structure based on a cubic $CsPbBr_3$ structure (for simplicity) where yellow shaded zone indicates the RP defect region. Decay associated spectra of Ac1 NCs in solution (d) and in thin-film (e) and of Et1 NCs in solution (f) and in thin-film (g) obtained by fit analysis of the photoluminescence decay traces recorded via TCSPC technique. Note that the accuracy of the 57-ns component is low due to the limited recorded time window of 50 ns. Fluorescence decay traces and their corresponding fits obtained for Ac1 (h) and Et1 (i) in solution and in

films via fs fluorescence up-conversion technique. The excitation wavelength was set to 360 nm; the detection wavelength is 510 nm.

In thin films, the PL decay of Ac1 is dominated by a 30.4 ns component (Fig. 4e), indicating that de-trapping of free carriers is the primary process responsible for photon emission (70 %), likely due to the presence of RP defects.[73] In contrast, this process plays only a minor role in solution, where it occurs with a time constant of 57 ns. Exciton recombination in the film, characterized by a 5.8 ns decay, contributes only 30 percent to the total emission. In sharp contrast, the luminescence of Et1 in film is primarily governed by exciton recombination, with time constants of 5.2 and 1.3 ns (Fig. 4g) and corresponding amplitudes of 50% and 20%, respectively. Radiative recombination of free carriers in Et1 films occurs with a similar time constant as in solution (21.2 ns). These results suggest that the enhanced luminescent properties of Et1 in film are due to the generation of a higher fraction of excitons, while the concentration of free carriers remains moderate.

Exciton formation dynamics play a crucial role in the design of perovskite materials with enhanced light-emission efficiency. The observed presence of excitonic species and their varying balance with free carriers prompted us to investigate the dynamics on a faster timescale using the femtosecond fluorescence up-conversion technique, which enables recording fluorescence decays with a temporal resolution of 100 fs. The decay traces and their corresponding fits are shown in Fig. S15-18, while Tables S7-8 summarize the extracted decay time constants and their relative contributions at different detection wavelengths. Measurements were conducted within a 50 ps time window following photoexcitation. A general trend can be observed: at shorter wavelengths, the fluorescence exhibits a rapid decay within the first 10 ps (positive amplitudes at 490 nm), while at longer wavelengths (510-630 nm), a rise in signal is observed (negative amplitudes), both characterized by identical time constants. This behavior indicates a strongly correlated dynamic process.

This spectroscopic signature provides strong evidence that the fast decay arises from relaxation processes in the conduction band, while the rising component corresponds to the population of relaxed excitonic states and the formation of bright exciton species. Specifically, the correlated decay and rise components of 2.1 ps observed for Ac1 in film and 2.4 ps for Et1 in film indicate that exciton formation is a relatively slow process (Fig. 4h,i). To verify this assignment, we conducted additional experiments by tuning the laser excitation wavelength to 360, 400, and 480 nm. In all cases, the exciton formation dynamics remained unchanged (data not shown), supporting the attribution of these time constants to exciton formation. Interestingly, exciton formation occurs more rapidly in solution, 1.4 ps for Ac1 and 1.1 ps for Et1, than in thin film, where the corresponding values are 2.1 ps and 2.3 ps, respectively (Fig. 4h,i). As previously reported, the exciton formation rate is primarily governed by the strength of the Coulomb interaction, which is reflected in the exciton binding energy.[83] A larger binding energy leads to a faster formation rate, implying that excitons in solution possess higher binding energies than those in films. No sub-picosecond components were observed at short wavelengths, which may suggest that a fraction of free carriers recombine nonradiatively before forming excitons. Nonradiative recombination is expected to occur on the fastest timescales. Once excitons are formed, the femtosecond fluorescence up-conversion measurements reveal processes with time constants of 4.7 ps and 15-20 ps for both Ac1 and Et1. These can be attributed to exciton relaxation phenomena and/or biexciton recombination.[45] Additionally, the decay traces and fit analyses include time components that are comparable to or exceed the experimental time window and are therefore poorly resolved here, though they were clearly detected in the TC-SPC experiments discussed earlier (vide infra).

Another consequence of defect formation, either on surface and in lattice is the PL blinking phenomenon observed in NCs.[84–86] Defects introduce inter-band "trap" states that facilitate nonradiative (NR) recombination of photo-generated or injected charge carriers.[87–91] The dynamic activation and deactivation of these defects cause PL intermittency, or blinking, characterized by alternating high-intensity (ON) and background-level (OFF) emission states.[84–86] The OFF states correspond to NR

quenching of excitons through active traps, while the ON states reflect radiative recombination. Additionally, crystal defects are known to trigger material degradation,[92] which ultimately compromises the photo-stability of the NCs.[93] Wide-field microscopy measurements (see Experimental Section in SI) at different excitation powers (488 nm laser at 0.36 μW/cm², 1.36 μW/cm², and 4.31 μW/cm²) under ambient conditions reveal that most Ac1 NCs exhibit frequent PL blinking (Fig. 5a, lower panel), indicating the presence of crystal defects and transiently active NR trap states. Furthermore, Ac1 NCs show significant (and in some cases complete) photo-bleaching to background levels (<45 counts per 30 ms) with increasing laser power. The blinking behavior can be attributed to RP defects and the exposure of the NC surface, which becomes ligand-free after Ac-based washing, leading to photo- and environment-induced degradation. In contrast, spatially separated CPB and Et1 single emitters are mostly observed (Fig. S19), whereas Ac1 NCs exhibit clear clustering behavior (Fig. S20). Representative regions of interest on CPB, Et1, and Ac1 thin films with ten marked, spatially isolated emitters from each system and their corresponding blinking traces are shown in Fig. S21-23. Unlike Ac1, CPB NCs do not exhibit blinking under any excitation power tested (Fig. 5a, top panel), suggesting the absence of NR defects[94] due to extensive ligand coverage. Similar non-blinking behavior is observed for Et1 NCs (Fig. 5a, middle panel), indicating that most ligands remain intact after ethyl acetate washing resulting defect-free structure. This results in exceptional photo-stability of both CPB and Et1 NCs, even under high laser power, and leads to a gradual enhancement of their PL intensity over time. Nonetheless, the moderate PLQYs observed across all NC samples suggest the presence of static quenchers in addition to the NR dynamic traps.

While Ac1 NCs typically undergo photo-bleaching and material degradation, a few emitters remained active under sequentially increasing laser power and displayed ON-OFF-ON blinking behavior during each excitation cycle (Fig. 5b, lower panel). To analyze this behavior, we performed a two-state blinking analysis on these Ac1 NCs at a medium excitation power of 1.36 μW/cm² and compared the results with those from CPB and Et1 NCs. The blinking characteristics of Ac1 NCs are reflected in a double-Gaussian

(DG) intensity distribution. In this case, the Gaussian peak near the background level represents the contribution of the OFF states. Interestingly, for CPB and Et1 NCs (Fig. 5b, top and middle panels), the DG converges into a single-Gaussian (SG) distribution at the high-intensity end, with no evidence of background-level OFF states. Based on the nature of the PL intensity distribution, we applied flexible thresholding to the blinking traces using the intensity histogram-dependent thresholding (IHDT) methodology.[86] For SG-type distributions of CPB and Et1 NCs, a single threshold (T_S) was used. In contrast, multiple thresholds (T_{ON} and T_{OFF}) were applied to the DG distributions of Ac1 NCs to distinguish the ON, OFF, and intermediate GREY states. The threshold positions for representative trajectories are shown in Fig. 5b (dotted lines). We then simulated the blinking trajectories using these thresholds: CPB and Et1 NCs were classified into ON ($PL \geq T_S$) and OFF ($PL \leq T_S$) states, while for Ac1 NCs, an additional GREY state ($T_{ON} \leq PL \leq T_{OFF}$) was identified. Based on these classifications, we calculated the "ON fraction" (%ON), excluding GREY state durations for Ac1 emitters.[86] The analysis shows that the %ON is approximately 90% for highly emissive CPB and Et1 NCs, while it drops significantly to around 46% for Ac1 NCs due to extended OFF durations. This trend holds for the majority of observed emitters. However, a few Et1 NCs exhibit brief OFF events under high excitation power presumably due non-solvent induced defects (Fig. S22).

Finally, to gain insight into the blinking dynamics, we constructed ON and OFF time distributions ($P(t_{On/Off})$) on a log-log scale based on the simulated trajectories, excluding the GREY states. These distributions were fitted using a (truncated) power-law model. For both CPB and Et1 NCs, the $P(t_{On})$ distributions exhibit truncation, with ON durations that are nearly two orders of magnitude longer than the corresponding OFF durations observed in $P(t_{Off})$, as shown in Fig. 5c,d. In contrast, Ac1 NCs display power-law (or near power-law) behavior in both ON and OFF time distributions, with comparable durations for each state in the blinking trajectories (Fig. 5e). These findings support our conclusion that long-lived non-radiative traps and defects are prevalent in Ac1 NCs. This highlights the crucial influence of solvent polarity during the washing process on the resulting optical quality of the NCs.

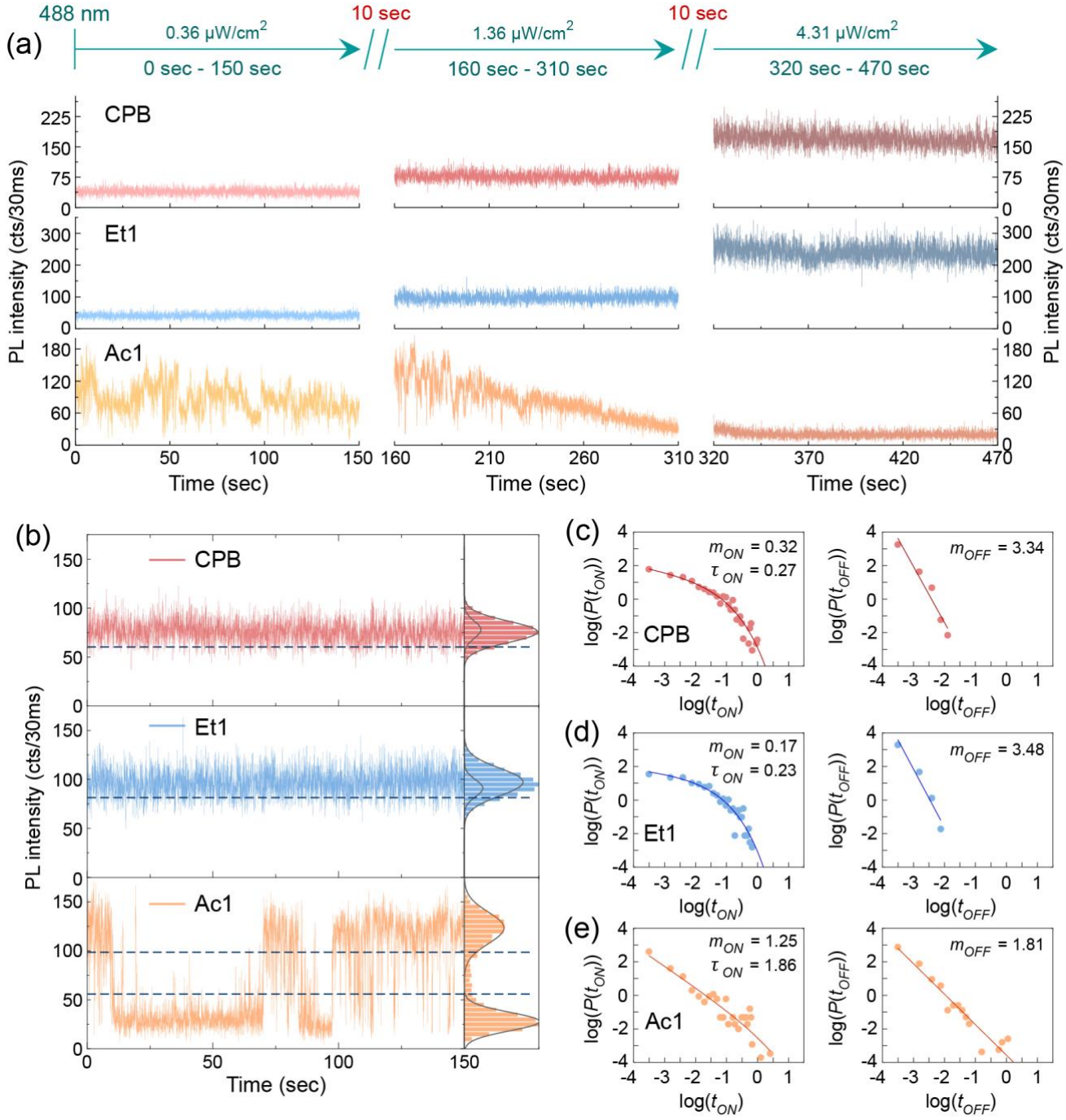


Figure 5: (a) The representative PL blinking trajectories of CPB, Ac1 and Et1 NCs are shown with their intensity distributions (in right panels). The intensity threshold(s) are represented with black dashed lines as calculated from the IHDT methodology. (b) Respective ON and OFF time distributions are fitted with linear and truncated power-law and fitting parameters are displayed. (c-e) The (laser) power-dependent changes in PL blinking behaviour of the CPB, Ac1 and Et1 NCs are represented in (b), where the power was altered with an interval of 10s.

To assess the impact of non-solvent purification on the optoelectronic properties of isolated $CsPbBr_3$ NCs, we fabricated proof-of-concept LEDs using CPB, Ac1, and Et1 NCs. The PeLED architecture consists of glass/ITO/PEDOT/PVK/NCs/PO-T2T/LiF/Al, where PEDOT, PVK, and PO-T2T refer to poly(3,4-ethylene dioxythiophene), polyvinylcarbazole, and 2,4,6-tris[3-(diphenylphosphinyl)phenyl]-1,3,5-triazine, respectively (Fig. 6a, inset schematic).[32,95–97] A representative SEM cross-section image confirms the layered structure of the fabricated device (Fig. S24a). The energy level alignment of the functional layers ensures balanced hole and electron injection into the NC emissive layer.[32] The devices fabricated with Et1 NCs exhibit electroluminescence at 515 nm, closely matching their PL spectra. Fig. 6a compares the luminance and current density for LEDs constructed from differently purified $CsPbBr_3$ NCs. All devices exhibit a similar turn-on voltage (~3.7 V) (Fig. S24b,c).[32,98] However, the Et1-based device reaches a maximum luminance of ~4069.8 cd/m² at 6 V, whereas the Ac1-based device achieves only ~7.1 cd/m² under the same bias (Fig. 6b, and Table S9). This reduced luminance is indicative of an emissive layer with a high density of non-radiative recombination centers, likely caused by surface and bulk defects that promote electron trapping. Et1 also demonstrates a two-fold higher external quantum efficiency (EQE) of 17.6% compared to Ac1 (8.1%) (Fig. 6c). Furthermore, the poor performance of pristine CPB NCs devices is likely due to inefficient charge injection, stemming from the high density of long-chain surface ligands that act as insulating barriers, impeding carrier transport. In contrast, the reduced performance of Ac1 devices is attributed to non-radiative recombination at planar RP defects, which likely originate from fractal structures formed during acetone washing. The enhanced performance of Et1-based devices can be ascribed to ethyl acetate purification, which likely promotes partial replacement of native oleate ligands with acetate anions. This ligand exchange reduces the density of long-chain insulating species on the NC surface, thereby improving carrier mobility. Upon aging the Et1-based LED for 1 day, the EQE decreases to ~15.1%, accompanied by an increase in current density and a drop in luminance. While further optimization is required to improve operational stability, the use of Et as a washing solvent appears to mitigate rapid device degradation, likely due to the formation of a less

defective perovskite emissive layer. These findings clearly demonstrate the significant role of polar non-solvent purification in balancing surface defect passivation and charge injection efficiency, ultimately enhancing the optoelectronic performance of $CsPbBr_3$ NC-based LEDs.

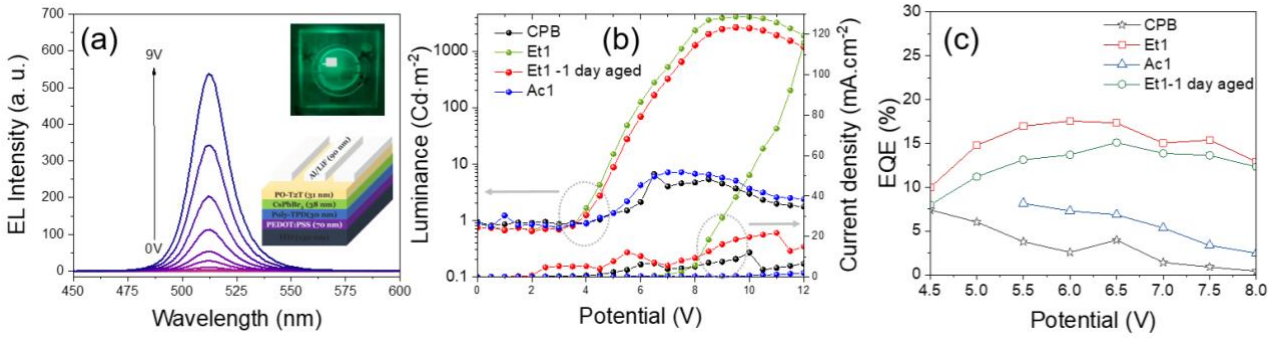


Figure 6. (a) Voltage dependent EL spectra of Et1 LED device. Inset show a photograph of the green emitting device (top panel) and the schematic of LED device stacks (bottom panel) used for the fabrication of $CsPbBr_3$ NCs LEDs. (b) Current, luminance and (c) EQE of CPB, Et1 and Ac1 devices.

CONCLUSION. This study demonstrates the dynamics of post-processing purification of $CsPbBr_3$ NCs required to reach excellent properties. Our results confirm that the purification step controls the amount and nature of the surface ligands as well as influences the morphology of the final product, depending also on the amount of the non-solvent used. Through combined XPS and NMR study it was shown that Ac-washing leads to appearance of more defective perovskite surface, while Et-washing results in the surface ligand exchange process from OL to acetate anions. *In-situ* SAXS measurements further showed that Ac leads to a faster aggregated bulk state than Et, for both non-solvents there is an *in-situ* formation of turbostratic stacked self-assemble intermediates. From systematic TEM measurements, we have observed extensive agglomeration of Ac-washed NCs with prominent RP faults formed. Time-resolved photoluminescence measurements revealed markedly different exciton formation and recombination dynamics processes across fs-ns timescales of differently washed NCs. Time-resolved spectroscopy shows the enhanced luminescent properties for Et1 due to the generation of a larger fraction of excitons,

whereas for Ac1 de-trapping of free carriers is the dominant process. This was further verified from the PL blinking experiment, where Ac1 shows defect induce inter-band "trap" states assisted nonradiative recombination of photo-generated charge-carriers leading to the higher population of OFF state, where CPB and Et1 NCs remain largely in the ON state. Furthermore, the functionality in the form of LEDs corroborates well with the morphology and structural defects as well as spectroscopic properties of the differently washed colloidal $CsPbBr_3$ NCs.

References

(1) Li, J.; Xu, L.; Wang, T.; Song, J.; Chen, J.; Xue, J.; Dong, Y.; Cai, B.; Shan, Q.; Han, B.; Zeng, H. 50-Fold EQE Improvement up to 6.27% of Solution-Processed All-Inorganic Perovskite CsPbBr3 QLEDs via Surface Ligand Density Control. *Advanced Materials* **2017**, *29* (5), 1603885. https://doi.org/10.1002/adma.201603885.

(2) Akkerman, Q. A.; Gandini, M.; Di Stasio, F.; Rastogi, P.; Palazon, F.; Bertoni, G.; Ball, J. M.; Prato, M.; Petrozza, A.; Manna, L. Strongly Emissive Perovskite Nanocrystal Inks for High-Voltage Solar Cells. *Nat Energy* **2016**, *2* (2), 1–7. https://doi.org/10.1038/nenergy.2016.194.

(3) Ramasamy, P.; Lim, D.-H.; Kim, B.; Lee, S.-H.; Lee, M.-S.; Lee, J.-S. All-Inorganic Cesium Lead Halide Perovskite Nanocrystals for Photodetector Applications. *Chem. Commun.* **2016**, *52* (10), 2067–2070. https://doi.org/10.1039/C5CC08643D.

(4) Xu, Y.; Chen, Q.; Zhang, C.; Wang, R.; Wu, H.; Zhang, X.; Xing, G.; Yu, W. W.; Wang, X.; Zhang, Y.; Xiao, M. Two-Photon-Pumped Perovskite Semiconductor Nanocrystal Lasers. *J. Am. Chem. Soc.* **2016**, *138* (11), 3761–3768. https://doi.org/10.1021/jacs.5b12662.

(5) Li, X.; Wu, Y.; Zhang, S.; Cai, B.; Gu, Y.; Song, J.; Zeng, H. CsPbX3 Quantum Dots for Lighting and Displays: Room-Temperature Synthesis, Photoluminescence Superiorities, Underlying Origins and White Light-Emitting Diodes. *Adv. Funct. Mater.* **2016**, *26* (15), 2435–2445. https://doi.org/10.1002/adfm.201600109.

(6) Vescio, G.; Frieiro, J. L.; Gualdrón-Reyes, A. F.; Hernández, S.; Mora-Seró, I.; Garrido, B.; Cirera, A. High Quality Inkjet Printed-Emissive Nanocrystalline Perovskite CsPbBr3 Layers for Color Conversion Layer and LEDs Applications. *Advanced Materials Technologies* **2022**, *7* (7), 2101525. https://doi.org/10.1002/admt.202101525.

(7) Chen, Q.; Wu, J.; Ou, X.; Huang, B.; Almutlaq, J.; Zhumekenov, A. A.; Guan, X.; Han, S.; Liang, L.; Yi, Z.; Li, J.; Xie, X.; Wang, Y.; Li, Y.; Fan, D.; Teh, D. B. L.; All, A. H.; Mohammed, O. F.; Bakr, O. M.; Wu, T.; Bettinelli, M.; Yang, H.; Huang, W.; Liu, X. All-Inorganic Perovskite Nanocrystal Scintillators. *Nature* **2018**, *561* (7721), 88–93. https://doi.org/10.1038/s41586-018-0451-1.

(8) Xu, Y.-F.; Yang, M.-Z.; Chen, B.-X.; Wang, X.-D.; Chen, H.-Y.; Kuang, D.-B.; Su, C.-Y. A CsPbBr3 Perovskite Quantum Dot/Graphene Oxide Composite for Photocatalytic CO2 Reduction. *J. Am. Chem. Soc.* **2017**, *139* (16), 5660–5663. https://doi.org/10.1021/jacs.7b00489.

(9) Paul, S.; Das Adhikari, S.; Pareja-Rivera, C.; Masi, S.; Julián-López, B.; Martinez-Pastor, J. P.; Escuder, B.; Mora-Seró, I. Impact of Peptide-Based Supramolecular Gels on the Passivation and Optical Properties of CsPbBr3 Nanocrystals for Photocatalytic Dye Degradation in Water. *Advanced Optical Materials* **2025**, *13* (4), 2402270. https://doi.org/10.1002/adom.202402270.

(10) Debroye, E.; Yuan, H.; Bladt, E.; Baekelant, W.; Van der Auweraer, M.; Hofkens, J.; Bals, S.; Roeffaers, M. B. J. Facile Morphology-Controlled Synthesis of Organolead Iodide Perovskite Nanocrystals Using Binary Capping Agents. *ChemNanoMat* **2017**, *3* (4), 223–227. https://doi.org/10.1002/cnma.201700006.
(11) De Roo, J.; Ibáñez, M.; Geiregat, P.; Nedelcu, G.; Walravens, W.; Maes, J.; Martins, J. C.; Van Driessche, I.; Kovalenko, M. V.; Hens, Z. Highly Dynamic Ligand Binding and Light Absorption Coefficient of Cesium Lead Bromide Perovskite Nanocrystals. *ACS Nano* **2016**, *10* (2), 2071–2081. https://doi.org/10.1021/acsnano.5b06295.
(12) Fang, T.; Wang, T.; Li, X.; Dong, Y.; Bai, S.; Song, J. Perovskite QLED with an External Quantum Efficiency of over 21% by Modulating Electronic Transport. *Science Bulletin* **2021**, *66* (1), 36–43. https://doi.org/10.1016/j.scib.2020.08.025.
(13) Wang, Y.-K.; Yuan, F.; Dong, Y.; Li, J.-Y.; Johnston, A.; Chen, B.; Saidaminov, M. I.; Zhou, C.; Zheng, X.; Hou, Y.; Bertens, K.; Ebe, H.; Ma, D.; Deng, Z.; Yuan, S.; Chen, R.; Sagar, L. K.; Liu, J.; Fan, J.; Li, P.; Li, X.; Gao, Y.; Fung, M.-K.; Lu, Z.-H.; Bakr, O. M.; Liao, L.-S.; Sargent, E. H. All-Inorganic Quantum-Dot LEDs Based on a Phase-Stabilized α-CsPbI3 Perovskite. *Angewandte Chemie International Edition* **2021**, *60* (29), 16164–16170. https://doi.org/10.1002/anie.202104812.
(14) Yao, J.-S.; Zhang, J.-C.; Wang, L.; Wang, K.-H.; Ru, X.-C.; Yang, J.-N.; Wang, J.-J.; Chen, X.; Song, Y.-H.; Yin, Y.-C.; Lan, Y.-F.; Zhang, Q.; Yao, H.-B. Suppressing Auger Recombination in Cesium Lead Bromide Perovskite Nanocrystal Film for Bright Light-Emitting Diodes. *J. Phys. Chem. Lett.* **2020**, *11* (21), 9371–9378. https://doi.org/10.1021/acs.jpclett.0c02777.
(15) Ghosh, S.; Pradhan, B.; Lin, W.; Zhang, Y.; Leoncino, L.; Chabera, P.; Zheng, K.; Solano, E.; Hofkens, J.; Pullerits, T. Slower Auger Recombination in 12-Faceted Dodecahedron CsPbBr3 Nanocrystals. *J. Phys. Chem. Lett.* **2023**, *14* (4), 1066–1072. https://doi.org/10.1021/acs.jpclett.2c03389.
(16) Kuang, Y.; Zhu, C.; He, W.; Wang, X.; He, Y.; Ran, X.; Guo, L. Regulated Exciton Dynamics and Optical Properties of Single Perovskite CsPbBr3 Quantum Dots by Diluting Surface Ligands. *J. Phys. Chem. C* **2020**, *124* (43), 23905–23912. https://doi.org/10.1021/acs.jpcc.0c05784.
(17) Kim, Y.; Yassitepe, E.; Voznyy, O.; Comin, R.; Walters, G.; Gong, X.; Kanjanaboos, P.; Nogueira, A. F.; Sargent, E. H. Efficient Luminescence from Perovskite Quantum Dot Solids. *ACS Appl. Mater. Interfaces* **2015**, *7* (45), 25007–25013. https://doi.org/10.1021/acsami.5b09084.
(18) Bodnarchuk, M. I.; Boehme, S. C.; ten Brinck, S.; Bernasconi, C.; Shynkarenko, Y.; Krieg, F.; Widmer, R.; Aeschlimann, B.; Günther, D.; Kovalenko, M. V.; Infante, I. Rationalizing and Controlling the Surface Structure and Electronic Passivation of Cesium Lead Halide Nanocrystals. *ACS Energy Lett.* **2019**, *4* (1), 63–74. https://doi.org/10.1021/acsenergylett.8b01669.
(19) Boles, M. A.; Engel, M.; Talapin, D. V. Self-Assembly of Colloidal Nanocrystals: From Intricate Structures to Functional Materials. *Chem. Rev.* **2016**, *116* (18), 11220–11289. https://doi.org/10.1021/acs.chemrev.6b00196.
(20) Protesescu, L.; Yakunin, S.; Bodnarchuk, M. I.; Krieg, F.; Caputo, R.; Hendon, C. H.; Yang, R. X.; Walsh, A.; Kovalenko, M. V. Nanocrystals of Cesium Lead Halide Perovskites (CsPbX3, X = Cl, Br, and I): Novel Optoelectronic Materials Showing Bright Emission with Wide Color Gamut. *Nano Lett.* **2015**, *15* (6), 3692–3696. https://doi.org/10.1021/nl5048779.
(21) van der Stam, W.; Geuchies, J. J.; Altantzis, T.; van den Bos, K. H. W.; Meeldijk, J. D.; Van Aert, S.; Bals, S.; Vanmaekelbergh, D.; de Mello Donega, C. Highly Emissive Divalent-Ion-Doped Colloidal CsPb1–xMxBr3 Perovskite Nanocrystals through Cation Exchange. *J. Am. Chem. Soc.* **2017**, *139* (11), 4087–4097. https://doi.org/10.1021/jacs.6b13079.
(22) Brennan, M. C.; Herr, J. E.; Nguyen-Beck, T. S.; Zinna, J.; Draguta, S.; Rouvimov, S.; Parkhill, J.; Kuno, M. Origin of the Size-Dependent Stokes Shift in CsPbBr3 Perovskite Nanocrystals. *J. Am. Chem. Soc.* **2017**, *139* (35), 12201–12208. https://doi.org/10.1021/jacs.7b05683.

(23) Nenon, D. P.; Pressler, K.; Kang, J.; Koscher, B. A.; Olshansky, J. H.; Osowiecki, W. T.; Koc, M. A.; Wang, L.-W.; Alivisatos, A. P. Design Principles for Trap-Free CsPbX3 Nanocrystals: Enumerating and Eliminating Surface Halide Vacancies with Softer Lewis Bases. *J. Am. Chem. Soc.* **2018**, *140* (50), 17760–17772. https://doi.org/10.1021/jacs.8b11035.
(24) Baranov, D.; Fieramosca, A.; Yang, R. X.; Polimeno, L.; Lerario, G.; Toso, S.; Giansante, C.; Giorgi, M. D.; Tan, L. Z.; Sanvitto, D.; Manna, L. Aging of Self-Assembled Lead Halide Perovskite Nanocrystal Superlattices: Effects on Photoluminescence and Energy Transfer. *ACS Nano* **2021**, *15* (1), 650–664. https://doi.org/10.1021/acsnano.0c06595.
(25) Dong, Y.; Wang, Y.-K.; Yuan, F.; Johnston, A.; Liu, Y.; Ma, D.; Choi, M.-J.; Chen, B.; Chekini, M.; Baek, S.-W.; Sagar, L. K.; Fan, J.; Hou, Y.; Wu, M.; Lee, S.; Sun, B.; Hoogland, S.; Quintero-Bermudez, R.; Ebe, H.; Todorovic, P.; Dinic, F.; Li, P.; Kung, H. T.; Saidaminov, M. I.; Kumacheva, E.; Spiecker, E.; Liao, L.-S.; Voznyy, O.; Lu, Z.-H.; Sargent, E. H. Bipolar-Shell Resurfacing for Blue LEDs Based on Strongly Confined Perovskite Quantum Dots. *Nat. Nanotechnol.* **2020**, *15* (8), 668–674. https://doi.org/10.1038/s41565-020-0714-5.
(26) Kumawat, N. K.; Swarnkar, A.; Nag, A.; Kabra, D. Ligand Engineering to Improve the Luminance Efficiency of CsPbBr3 Nanocrystal Based Light-Emitting Diodes. *J. Phys. Chem. C* **2018**, *122* (25), 13767–13773. https://doi.org/10.1021/acs.jpcc.8b00723.
(27) Ye, J.; Li, Z.; Kubicki, D. J.; Zhang, Y.; Dai, L.; Otero-Martínez, C.; Reus, M. A.; Arul, R.; Dudipala, K. R.; Andaji-Garmaroudi, Z.; Huang, Y.-T.; Li, Z.; Chen, Z.; Müller-Buschbaum, P.; Yip, H.-L.; Stranks, S. D.; Grey, C. P.; Baumberg, J. J.; Greenham, N. C.; Polavarapu, L.; Rao, A.; Hoye, R. L. Z. Elucidating the Role of Antisolvents on the Surface Chemistry and Optoelectronic Properties of CsPbBrxI3-x Perovskite Nanocrystals. *J. Am. Chem. Soc.* **2022**, *144* (27), 12102–12115. https://doi.org/10.1021/jacs.2c02631.
(28) Yuan, L.; Patterson, R.; Wen, X.; Zhang, Z.; Conibeer, G.; Huang, S. Investigation of Anti-Solvent Induced Optical Properties Change of Cesium Lead Bromide Iodide Mixed Perovskite (CsPbBr3-xIx) Quantum Dots. *Journal of Colloid and Interface Science* **2017**, *504* (Supplement C), 586–592. https://doi.org/10.1016/j.jcis.2017.06.017.
(29) Hoshi, K.; Chiba, T.; Sato, J.; Hayashi, Y.; Takahashi, Y.; Ebe, H.; Ohisa, S.; Kido, J. Purification of Perovskite Quantum Dots Using Low-Dielectric-Constant Washing Solvent "Diglyme" for Highly Efficient Light-Emitting Devices. *ACS Appl. Mater. Interfaces* **2018**, *10* (29), 24607–24612. https://doi.org/10.1021/acsami.8b05954.
(30) Raja, S. N.; Bekenstein, Y.; Koc, M. A.; Fischer, S.; Zhang, D.; Lin, L.; Ritchie, R. O.; Yang, P.; Alivisatos, A. P. Encapsulation of Perovskite Nanocrystals into Macroscale Polymer Matrices: Enhanced Stability and Polarization. *ACS Appl. Mater. Interfaces* **2016**, *8* (51), 35523–35533. https://doi.org/10.1021/acsami.6b09443.
(31) Akkerman, Q. A.; D'Innocenzo, V.; Accornero, S.; Scarpellini, A.; Petrozza, A.; Prato, M.; Manna, L. Tuning the Optical Properties of Cesium Lead Halide Perovskite Nanocrystals by Anion Exchange Reactions. *J. Am. Chem. Soc.* **2015**, *137* (32), 10276–10281. https://doi.org/10.1021/jacs.5b05602.
(32) Zhang, Y.; Chouhan, L.; Fron, E.; Leoncino, L.; Elkhouly, K.; Bhatia, H.; Qiu, W.; Roeffaers, M. B. J.; Hofkens, J.; Debroye, E.; Pradhan, B. Operationally Stable and Efficient CsPbI3–xBrx Perovskite Nanocrystal Light-Emitting Diodes Enabled by Ammonium Ligand Surface Treatment. *ACS Photonics* **2023**, *10* (8), 2774–2783. https://doi.org/10.1021/acsphotonics.3c00480.
(33) Akkerman, Q. A.; Nguyen, T. P. T.; Boehme, S. C.; Montanarella, F.; Dirin, D. N.; Wechsler, P.; Beiglböck, F.; Rainò, G.; Erni, R.; Katan, C.; Even, J.; Kovalenko, M. V. Controlling the Nucleation and Growth Kinetics of Lead Halide Perovskite Quantum Dots. *Science* **2022**, *377* (6613), 1406–1412. https://doi.org/10.1126/science.abq3616.
(34) Pan, J.; Quan, L. N.; Zhao, Y.; Peng, W.; Murali, B.; Sarmah, S. P.; Yuan, M.; Sinatra, L.; Alyami, N. M.; Liu, J.; Yassitepe, E.; Yang, Z.; Voznyy, O.; Comin, R.; Hedhili, M. N.; Mohammed, O. F.; Lu, Z. H.; Kim, D. H.; Sargent, E. H.; Bakr, O. M. Highly Efficient Perovskite-Quantum-Dot

Light-Emitting Diodes by Surface Engineering. *Adv. Mater.* **2016**, *28* (39), 8718–8725. https://doi.org/10.1002/adma.201600784.
(35) Krieg, F.; Ong, Q. K.; Burian, M.; Rainò, G.; Naumenko, D.; Amenitsch, H.; Süess, A.; Grotevent, M. J.; Krumeich, F.; Bodnarchuk, M. I.; Shorubalko, I.; Stellacci, F.; Kovalenko, M. V. Stable Ultraconcentrated and Ultradilute Colloids of CsPbX3 (X = Cl, Br) Nanocrystals Using Natural Lecithin as a Capping Ligand. *J. Am. Chem. Soc.* **2019**, *141* (50), 19839–19849. https://doi.org/10.1021/jacs.9b09969.
(36) Krieg, F.; Sercel, P. C.; Burian, M.; Andrusiv, H.; Bodnarchuk, M. I.; Stöferle, T.; Mahrt, R. F.; Naumenko, D.; Amenitsch, H.; Rainò, G.; Kovalenko, M. V. Monodisperse Long-Chain Sulfobetaine-Capped CsPbBr3 Nanocrystals and Their Superfluorescent Assemblies. *ACS Cent. Sci.* **2021**, *7* (1), 135–144. https://doi.org/10.1021/acscentsci.0c01153.
(37) Morrell, M. V.; He, X.; Luo, G.; Thind, A. S.; White, T. A.; Hachtel, J. A.; Borisevich, A. Y.; Idrobo, J.-C.; Mishra, R.; Xing, Y. Significantly Enhanced Emission Stability of CsPbBr3 Nanocrystals via Chemically Induced Fusion Growth for Optoelectronic Devices. *ACS Appl. Nano Mater.* **2018**, *1* (11), 6091–6098. https://doi.org/10.1021/acsanm.8b01298.
(38) Ripka, E. G.; Deschene, C. R.; Franck, J. M.; Bae, I.-T.; Maye, M. M. Understanding the Surface Properties of Halide Exchanged Cesium Lead Halide Nanoparticles. *Langmuir* **2018**, *34* (37), 11139–11146. https://doi.org/10.1021/acs.langmuir.8b02148.
(39) Jing, Q.; Zhang, M.; Huang, X.; Ren, X.; Wang, P.; Lu, Z. Surface Passivation of Mixed-Halide Perovskite CsPb(BrxI1−x)3 Nanocrystals by Selective Etching for Improved Stability. *Nanoscale* **2017**, *9* (22), 7391–7396. https://doi.org/10.1039/C7NR01287J.
(40) Wheeler, L. M.; Sanehira, E. M.; Marshall, A. R.; Schulz, P.; Suri, M.; Anderson, N. C.; Christians, J. A.; Nordlund, D.; Sokaras, D.; Kroll, T.; Harvey, S. P.; Berry, J. J.; Lin, L. Y.; Luther, J. M. Targeted Ligand-Exchange Chemistry on Cesium Lead Halide Perovskite Quantum Dots for High-Efficiency Photovoltaics. *J. Am. Chem. Soc.* **2018**, *140* (33), 10504–10513. https://doi.org/10.1021/jacs.8b04984.
(41) Chen, C.; Wu, Y.; Liu, L.; Gao, Y.; Chen, X.; Bi, W.; Chen, X.; Liu, D.; Dai, Q.; Song, H. Interfacial Engineering and Photon Downshifting of CsPbBr3 Nanocrystals for Efficient, Stable, and Colorful Vapor Phase Perovskite Solar Cells. *Advanced Science* **2019**, *6* (11), 1802046. https://doi.org/10.1002/advs.201802046.
(42) Zheng, W.; Wan, Q.; Liu, M.; Zhang, Q.; Zhang, C.; Yan, R.; Feng, X.; Kong, L.; Li, L. CsPbBr3 Nanocrystal Light-Emitting Diodes with Efficiency up to 13.4% Achieved by Careful Surface Engineering and Device Engineering. *J. Phys. Chem. C* **2021**, *125* (5), 3110–3118. https://doi.org/10.1021/acs.jpcc.0c11085.
(43) Wang, H.; Ye, F.; Sun, J.; Wang, Z.; Zhang, C.; Qian, J.; Zhang, X.; Choy, W. C. H.; Sun, X. W.; Wang, K.; Zhao, W. Efficient CsPbBr3 Nanoplatelet-Based Blue Light-Emitting Diodes Enabled by Engineered Surface Ligands. *ACS Energy Lett.* **2022**, *7* (3), 1137–1145. https://doi.org/10.1021/acsenergylett.1c02642.
(44) Becker, M. A.; Vaxenburg, R.; Nedelcu, G.; Sercel, P. C.; Shabaev, A.; Mehl, M. J.; Michopoulos, J. G.; Lambrakos, S. G.; Bernstein, N.; Lyons, J. L.; Stöferle, T.; Mahrt, R. F.; Kovalenko, M. V.; Norris, D. J.; Rainò, G.; Efros, A. L. Bright Triplet Excitons in Caesium Lead Halide Perovskites. *Nature* **2018**, *553* (7687), 189–193. https://doi.org/10.1038/nature25147.
(45) Ahumada-Lazo, R.; Saran, R.; Woolland, O.; Jia, Y.; Kyriazi, M.-E.; Kanaras, A. G.; Binks, D.; Curry, R. J. Exciton Effects in Perovskite Nanocrystals. *J. Phys. Photonics* **2021**, *3* (2), 021002. https://doi.org/10.1088/2515-7647/abedd0.
(46) Dang, Z.; Shamsi, J.; Palazon, F.; Imran, M.; Akkerman, Q. A.; Park, S.; Bertoni, G.; Prato, M.; Brescia, R.; Manna, L. In Situ Transmission Electron Microscopy Study of Electron Beam-Induced Transformations in Colloidal Cesium Lead Halide Perovskite Nanocrystals. *ACS Nano* **2017**, *11* (2), 2124–2132. https://doi.org/10.1021/acsnano.6b08324.

(47) Brennan, M. C.; Kuno, M.; Rouvimov, S. Crystal Structure of Individual CsPbBr3 Perovskite Nanocubes. *Inorg. Chem.* **2019**, *58* (2), 1555–1560. https://doi.org/10.1021/acs.inorgchem.8b03078.
(48) Zhang, D.; Eaton, S. W.; Yu, Y.; Dou, L.; Yang, P. Solution-Phase Synthesis of Cesium Lead Halide Perovskite Nanowires. *J. Am. Chem. Soc.* **2015**, *137* (29), 9230–9233. https://doi.org/10.1021/jacs.5b05404.
(49) Kirschner, M. S.; Diroll, B. T.; Guo, P.; Harvey, S. M.; Helweh, W.; Flanders, N. C.; Brumberg, A.; Watkins, N. E.; Leonard, A. A.; Evans, A. M.; Wasielewski, M. R.; Dichtel, W. R.; Zhang, X.; Chen, L. X.; Schaller, R. D. Photoinduced, Reversible Phase Transitions in All-Inorganic Perovskite Nanocrystals. *Nat Commun* **2019**, *10* (1), 504. https://doi.org/10.1038/s41467-019-08362-3.
(50) Calvin, J. J.; Kaufman, T. M.; Sedlak, A. B.; Crook, M. F.; Alivisatos, A. P. Observation of Ordered Organic Capping Ligands on Semiconducting Quantum Dots via Powder X-Ray Diffraction. *Nat Commun* **2021**, *12* (1), 2663. https://doi.org/10.1038/s41467-021-22947-x.
(51) Xing, Y.; Yazdani, N.; Lin, W. M. M.; Yarema, M.; Zahn, R.; Wood, V. Effect of Positional Disorders on Charge Transport in Nanocrystal Quantum Dot Thin Films. *ACS Appl. Electron. Mater.* **2022**, *4* (2), 631–642. https://doi.org/10.1021/acsaelm.1c01011.
(52) Wang, Y.-K.; Wan, H.; Teale, S.; Grater, L.; Zhao, F.; Zhang, Z.; Duan, H.-W.; Imran, M.; Wang, S.-D.; Hoogland, S.; Liao, L.-S. Long-Range Order Enabled Stability in Quantum Dot Light-Emitting Diodes. *Nature* **2024**, *629* (8012), 586–591. https://doi.org/10.1038/s41586-024-07363-7.
(53) Pradhan, B.; Mushtaq, A.; Roy, D.; Sain, S.; Das, B.; Ghorai, U. K.; Pal, S. K.; Acharya, S. Postsynthesis Spontaneous Coalescence of Mixed-Halide Perovskite Nanocubes into Phase-Stable Single-Crystalline Uniform Luminescent Nanowires. *J. Phys. Chem. Lett.* **2019**, *10* (8), 1805–1812. https://doi.org/10.1021/acs.jpclett.9b00832.
(54) Uribe-Vegas, P.; Villanueva-Antolí, A.; Segura, C.; Werlinger, F.; Aliaga, K. R.; Caprile, R.; Trofymchuk, O. S.; Flores, M. E.; Osorio-Román, I. O.; Echeverría-Arrondo, C.; Adhikari, S. D.; Selmi, O.; Seró, I. M.; Rodriguez-Pereira, J.; Pradhan, B.; Paulus, M.; Sternemann, C.; Hofkens, J.; Martinez, J.; Masi, S.; Gualdrón-Reyes, A. F. The Role of Alkylammonium Bromides on the Surface Passivation of Stable Alcohol-Dispersed CsPbX3 Nanocrystals and on the Stability Enhancement in Light-Emitting Applications. *Advanced Optical Materials* **2024**, *12* (31), 2401475. https://doi.org/10.1002/adom.202401475.
(55) Bhatia, H.; Martin, C.; Keshavarz, M.; Dovgaliuk, I.; Schrenker, N. J.; Ottesen, M.; Qiu, W.; Fron, E.; Bremholm, M.; Van de Vondel, J.; Bals, S.; Roeffaers, M. B. J.; Hofkens, J.; Debroye, E. Deciphering the Role of Water in Promoting the Optoelectronic Performance of Surface-Engineered Lead Halide Perovskite Nanocrystals. *ACS Appl. Mater. Interfaces* **2023**, *15* (5), 7294–7307. https://doi.org/10.1021/acsami.2c20605.
(56) Zhang, W.-X.; Chen, J.-S.; Liu, X.-P.; Mao, C.-J.; Jin, B.-K. An Electrochemiluminescent Sensor Based on Hydrophilic CsPbBr 3 /TDPA Nanocrystals for Sensitive Detection of Nitrobenzene. *Sensors & Diagnostics* **2023**, *2* (2), 445–456. https://doi.org/10.1039/D3SD00007A.
(57) Ravi, V. K.; Santra, P. K.; Joshi, N.; Chugh, J.; Singh, S. K.; Rensmo, H.; Ghosh, P.; Nag, A. Origin of the Substitution Mechanism for the Binding of Organic Ligands on the Surface of CsPbBr3 Perovskite Nanocubes. *J. Phys. Chem. Lett.* **2017**, *8* (20), 4988–4994. https://doi.org/10.1021/acs.jpclett.7b02192.
(58) Almeida, G.; Goldoni, L.; Akkerman, Q.; Dang, Z.; Khan, A. H.; Marras, S.; Moreels, I.; Manna, L. Role of Acid–Base Equilibria in the Size, Shape, and Phase Control of Cesium Lead Bromide Nanocrystals. *ACS Nano* **2018**, *12* (2), 1704–1711. https://doi.org/10.1021/acsnano.7b08357.
(59) Recalde, I.; Gualdrón-Reyes, Andrés. F.; Echeverría-Arrondo, C.; Villanueva-Antolí, A.; Simancas, J.; Rodriguez-Pereira, J.; Zanatta, M.; Mora-Seró, I.; Sans, V. Vitamins as Active Agents for Highly Emissive and Stable Nanostructured Halide Perovskite Inks and 3D Composites

Fabricated by Additive Manufacturing. *Advanced Functional Materials* **2023**, *33* (8), 2210802. https://doi.org/10.1002/adfm.202210802.
(60) Zickler, G. A.; Smarsly, B.; Gierlinger, N.; Peterlik, H.; Paris, O. A Reconsideration of the Relationship between the Crystallite Size *L*a of Carbons Determined by X-Ray Diffraction and Raman Spectroscopy. *Carbon* **2006**, *44* (15), 3239–3246. https://doi.org/10.1016/j.carbon.2006.06.029.
(61) Eichhorn, S.; Hearle, J. W. S.; Jaffe, M.; Kikutani, T. *Handbook of Textile Fibre Structure: Volume 2: Natural, Regenerated, Inorganic and Specialist Fibres*; Elsevier, 2009.
(62) Sun, J.-K.; Huang, S.; Liu, X.-Z.; Xu, Q.; Zhang, Q.-H.; Jiang, W.-J.; Xue, D.-J.; Xu, J.-C.; Ma, J.-Y.; Ding, J.; Ge, Q.-Q.; Gu, L.; Fang, X.; Zhong, H.-Z.; Hu, J.-S.; Wan, L.-J. Polar Solvent Induced Lattice Distortion of Cubic CsPbI3 Nanocubes and Hierarchical Self-Assembly into Orthorhombic Single-Crystalline Nanowires. *J. Am. Chem. Soc.* **2018**. https://doi.org/10.1021/jacs.8b05949.
(63) Lee, B.; Littrell, K.; Sha, Y.; Shevchenko, E. V. Revealing the Effects of the Non-Solvent on the Ligand Shell of Nanoparticles and Their Crystallization. *J. Am. Chem. Soc.* **2019**, *141* (42), 16651–16662. https://doi.org/10.1021/jacs.9b06010.
(64) Loubat, A.; Lacroix, L.-M.; Robert, A.; Impéror-Clerc, M.; Poteau, R.; Maron, L.; Arenal, R.; Pansu, B.; Viau, G. Ultrathin Gold Nanowires: Soft-Templating versus Liquid Phase Synthesis, a Quantitative Study. *J. Phys. Chem. C* **2015**, *119* (8), 4422–4430. https://doi.org/10.1021/acs.jpcc.5b00242.
(65) Rath, T.; Novák, J.; Amenitsch, H.; Pein, A.; Maier, E.; Haas, W.; Hofer, F.; Trimmel, G. Real Time X-Ray Scattering Study of the Formation of ZnS Nanoparticles Using Synchrotron Radiation. *Materials Chemistry and Physics* **2014**, *144* (3), 310–317. https://doi.org/10.1016/j.matchemphys.2013.12.045.
(66) Teixeira, J. Small-Angle Scattering by Fractal Systems. *Journal of Applied Crystallography* **1988**, *21* (6), 781–785. https://doi.org/10.1107/S0021889888000263.
(67) Dahlman, C. J.; Venkatesan, N. R.; Corona, P. T.; Kennard, R. M.; Mao, L.; Smith, N. C.; Zhang, J.; Seshadri, R.; Helgeson, M. E.; Chabinyc, M. L. Structural Evolution of Layered Hybrid Lead Iodide Perovskites in Colloidal Dispersions. *ACS Nano* **2020**, *14* (9), 11294–11308. https://doi.org/10.1021/acsnano.0c03219.
(68) Akkerman, Q. A.; Motti, S. G.; Srimath Kandada, A. R.; Mosconi, E.; D'Innocenzo, V.; Bertoni, G.; Marras, S.; Kamino, B. A.; Miranda, L.; De Angelis, F.; Petrozza, A.; Prato, M.; Manna, L. Solution Synthesis Approach to Colloidal Cesium Lead Halide Perovskite Nanoplatelets with Monolayer-Level Thickness Control. *J. Am. Chem. Soc.* **2016**, *138* (3), 1010–1016. https://doi.org/10.1021/jacs.5b12124.
(69) van der Burgt, J. S.; Geuchies, J. J.; van der Meer, B.; Vanrompay, H.; Zanaga, D.; Zhang, Y.; Albrecht, W.; Petukhov, A. V.; Filion, L.; Bals, S.; Swart, I.; Vanmaekelbergh, D. Cuboidal Supraparticles Self-Assembled from Cubic CsPbBr3 Perovskite Nanocrystals. *J. Phys. Chem. C* **2018**, *122* (27), 15706–15712. https://doi.org/10.1021/acs.jpcc.8b02699.
(70) De Backer, A.; van den Bos, K. H. W.; Van den Broek, W.; Sijbers, J.; Van Aert, S. StatSTEM: An Efficient Approach for Accurate and Precise Model-Based Quantification of Atomic Resolution Electron Microscopy Images. *Ultramicroscopy* **2016**, *171*, 104–116. https://doi.org/10.1016/j.ultramic.2016.08.018.
(71) Yu, Y.; Zhang, D.; Yang, P. Ruddlesden–Popper Phase in Two-Dimensional Inorganic Halide Perovskites: A Plausible Model and the Supporting Observations. *Nano Lett.* **2017**, *17* (9), 5489–5494. https://doi.org/10.1021/acs.nanolett.7b02146.
(72) Thind, A. S.; Luo, G.; Hachtel, J. A.; Morrell, M. V.; Cho, S. B.; Borisevich, A. Y.; Idrobo, J.-C.; Xing, Y.; Mishra, R. Atomic Structure and Electrical Activity of Grain Boundaries and Ruddlesden–Popper Faults in Cesium Lead Bromide Perovskite. *Advanced Materials* **2019**, *31* (4), 1805047. https://doi.org/10.1002/adma.201805047.

(73) Lee, A.; Park, J. H.; Kim, H.; Jeong, H. Y.; Lee, J. H.; Song, M. H. Blue Perovskite Nanocrystal Light-Emitting Diodes: Overcoming Ruddlesden□Popper Fault-Induced Nonradiative Recombination via Post-Halide Exchange. *Small* **2022**, *18* (52), 2205011. https://doi.org/10.1002/smll.202205011.
(74) Paul, S.; Bladt, E.; Richter, A. F.; Döblinger, M.; Tong, Y.; Huang, H.; Dey, A.; Bals, S.; Debnath, T.; Polavarapu, L.; Feldmann, J. Manganese-Doping-Induced Quantum Confinement within Host Perovskite Nanocrystals through Ruddlesden–Popper Defects. *Angewandte Chemie International Edition* **2020**, *59* (17), 6794–6799. https://doi.org/10.1002/anie.201914473.
(75) Imran, M.; Ramade, J.; Di Stasio, F.; De Franco, M.; Buha, J.; Van Aert, S.; Goldoni, L.; Lauciello, S.; Prato, M.; Infante, I.; Bals, S.; Manna, L. Alloy CsCdxPb1–xBr3 Perovskite Nanocrystals: The Role of Surface Passivation in Preserving Composition and Blue Emission. *Chem. Mater.* **2020**, *32* (24), 10641–10652. https://doi.org/10.1021/acs.chemmater.0c03825.
(76) Skvortsova, I.; Braeckevelt, T.; De Backer, A.; Schrenker, N.; Pradhan, B.; Hofkens, J.; Van Aert, S.; Van Speybroeck, V.; Bals, S. Increasing the Phase Stability of CsPbI3 Nanocrystals by Zn2+ and Cd2+ Addition: Synergy of Transmission Electron Microscopy and Molecular Dynamics. *ACS Nano* **2025**, *19* (18), 17698–17708. https://doi.org/10.1021/acsnano.5c01825.
(77) Pradhan, B.; Keshavarz, M.; Zhang, Y.; Sun, L.; Marquez, C.; Smolders, S.; De Vos, D.; Fron, E.; Van de Vondel, J.; Naumenko, D.; Amenitsch, H.; Debroye, E.; Roeffaers, M. B.; Hofkens, J. Mn Doping in Low-Dimensional Perovskites: A Switch for Controlling Dopant and Host Emission. *J. Phys. Chem. C* **2023**, *127* (22), 10629–10639. https://doi.org/10.1021/acs.jpcc.3c01774.
(78) Makarov, N. S.; Guo, S.; Isaienko, O.; Liu, W.; Robel, I.; Klimov, V. I. Spectral and Dynamical Properties of Single Excitons, Biexcitons, and Trions in Cesium–Lead-Halide Perovskite Quantum Dots. *Nano Lett.* **2016**, *16* (4), 2349–2362. https://doi.org/10.1021/acs.nanolett.5b05077.
(79) Chung, H.; Jung, S. I.; Kim, H. J.; Cha, W.; Sim, E.; Kim, D.; Koh, W.-K.; Kim, J. Composition-Dependent Hot Carrier Relaxation Dynamics in Cesium Lead Halide (CsPbX3, X=Br and I) Perovskite Nanocrystals. *Angewandte Chemie International Edition* **2017**, *56* (15), 4160–4164. https://doi.org/10.1002/anie.201611916.
(80) Mondal, N.; De, A.; Das, S.; Paul, S.; Samanta, A. Ultrafast Carrier Dynamics of Metal Halide Perovskite Nanocrystals and Perovskite-Composites. *Nanoscale* **2019**, *11* (20), 9796–9818. https://doi.org/10.1039/C9NR01745C.
(81) Chen, J.; Zhang, C.; Liu, X.; Peng, L.; Lin, J.; Chen, X. Carrier Dynamic Process in All-Inorganic Halide Perovskites Explored by Photoluminescence Spectra. *Photon. Res., PRJ* **2021**, *9* (2), 151–170. https://doi.org/10.1364/PRJ.410290.
(82) Sun, Q.; Zhao, C.; Yin, Z.; Wang, S.; Leng, J.; Tian, W.; Jin, S. Ultrafast and High-Yield Polaronic Exciton Dissociation in Two-Dimensional Perovskites. *J. Am. Chem. Soc.* **2021**, *143* (45), 19128–19136. https://doi.org/10.1021/jacs.1c08900.
(83) Sarritzu, V.; Sestu, N.; Marongiu, D.; Chang, X.; Wang, Q.; Loi, M. A.; Quochi, F.; Saba, M.; Mura, A.; Bongiovanni, G. Perovskite Excitonics: Primary Exciton Creation and Crossover from Free Carriers to a Secondary Exciton Phase. *Advanced Optical Materials* **2018**, *6* (3), 1700839. https://doi.org/10.1002/adom.201700839.
(84) Nirmal, M.; Dabbousi, B. O.; Bawendi, M. G.; Macklin, J. J.; Trautman, J. K.; Harris, T. D.; Brus, L. E. Fluorescence Intermittency in Single Cadmium Selenide Nanocrystals. *Nature* **1996**, *383* (6603), 802–804. https://doi.org/10.1038/383802a0.
(85) Kuno, M.; Fromm, D. P.; Hamann, H. F.; Gallagher, A.; Nesbitt, D. J. Nonexponential "Blinking" Kinetics of Single CdSe Quantum Dots: A Universal Power Law Behavior. *The Journal of Chemical Physics* **2000**, *112* (7), 3117–3120. https://doi.org/10.1063/1.480896.
(86) Mukherjee, A.; Ray, K. K.; Phadnis, C.; Layek, A.; Bera, S.; Chowdhury, A. Insights on Heterogeneity in Blinking Mechanisms and Non-Ergodicity Using Sub-Ensemble Statistical Analysis of Single Quantum-Dots. *The Journal of Chemical Physics* **2019**, *151* (8), 084701. https://doi.org/10.1063/1.5095870.

(87) Jin, H.; Debroye, E.; Keshavarz, M.; Scheblykin, I. G.; Roeffaers, M. B. J.; Hofkens, J.; Steele, J. A. It's a Trap! On the Nature of Localised States and Charge Trapping in Lead Halide Perovskites. *Mater. Horiz.* **2020**, *7* (2), 397–410. https://doi.org/10.1039/C9MH00500E.
(88) Merdasa, A.; Tian, Y.; Camacho, R.; Dobrovolsky, A.; Debroye, E.; Unger, E. L.; Hofkens, J.; Sundström, V.; Scheblykin, I. G. "Supertrap" at Work: Extremely Efficient Nonradiative Recombination Channels in MAPbI3 Perovskites Revealed by Luminescence Super-Resolution Imaging and Spectroscopy. *ACS Nano* **2017**, *11* (6), 5391–5404. https://doi.org/10.1021/acsnano.6b07407.
(89) Gerhard, M.; Louis, B.; Camacho, R.; Merdasa, A.; Li, J.; Kiligaridis, A.; Dobrovolsky, A.; Hofkens, J.; Scheblykin, I. G. Microscopic Insight into Non-Radiative Decay in Perovskite Semiconductors from Temperature-Dependent Luminescence Blinking. *Nat Commun* **2019**, *10* (1), 1698. https://doi.org/10.1038/s41467-019-09640-w.
(90) Yuan, H.; Debroye, E.; Caliandro, G.; Janssen, K. P. F.; van Loon, J.; Kirschhock, C. E. A.; Martens, J. A.; Hofkens, J.; Roeffaers, M. B. J. Photoluminescence Blinking of Single-Crystal Methylammonium Lead Iodide Perovskite Nanorods Induced by Surface Traps. *ACS Omega* **2016**, *1* (1), 148–159. https://doi.org/10.1021/acsomega.6b00107.
(91) Jin, H.; Steele, J. A.; Cheng, R.; Parveen, N.; Roeffaers, M. B. J.; Hofkens, J.; Debroye, E. Experimental Evidence of Chloride-Induced Trap Passivation in Lead Halide Perovskites through Single Particle Blinking Studies. *Advanced Optical Materials* **2021**, *9* (23), 2002240. https://doi.org/10.1002/adom.202002240.
(92) Kwak, K.; Lim, E.; Ahn, N.; Heo, J.; Bang, K.; Kim, S. K.; Choi, M. An Atomistic Mechanism for the Degradation of Perovskite Solar Cells by Trapped Charge. *Nanoscale* **2019**, *11* (23), 11369–11378. https://doi.org/10.1039/C9NR02193K.
(93) Mukherjee, A.; Roy, M.; Pathoor, N.; Aslam, M.; Chowdhury, A. Influence of Atmospheric Constituents on Spectral Instability and Defect-Mediated Carrier Recombination in Hybrid Perovskite Nanoplatelets. *J. Phys. Chem. C* **2021**, *125* (31), 17133–17143. https://doi.org/10.1021/acs.jpcc.1c02207.
(94) Praneeth, N. V. S.; Akhil, S.; Mukherjee, A.; Seth, S.; Khatua, S.; Mishra, N. Amine-Free Multi-Faceted CsPbBr3 Nanocrystals for Complete Suppression of Long-Lived Dark States. *Advanced Optical Materials* **2024**, *12* (16), 2303222. https://doi.org/10.1002/adom.202303222.
(95) Bhatia, H.; Steele, J. A.; Martin, C.; Keshavarz, M.; Solis-Fernandez, G.; Yuan, H.; Fleury, G.; Huang, H.; Dovgaliuk, I.; Chernyshov, D.; Hendrix, J.; Roeffaers, M. B. J.; Hofkens, J.; Debroye, E. Single-Step Synthesis of Dual Phase Bright Blue-Green Emitting Lead Halide Perovskite Nanocrystal Thin Films. *Chem. Mater.* **2019**, *31* (17), 6824–6832. https://doi.org/10.1021/acs.chemmater.9b01277.
(96) Zhang, Y.; Keshavarz, M.; Debroye, E.; Fron, E.; González, M. C. R.; Naumenko, D.; Amenitsch, H.; Vondel, J. V. de; Feyter, S. D.; Heremans, P.; Roeffaers, M. B. J.; Qiu, W.; Pradhan, B.; Hofkens, J. Two-Dimensional Perovskites with Alternating Cations in the Interlayer Space for Stable Light-Emitting Diodes. *Nanophotonics* **2020**, *10* (8), 2145–2156. https://doi.org/10.1515/nanoph-2021-0037.
(97) Zhang, Y.; Chen, J. J.-K.; Fron, E.; Bazylevska, A.; Wang, P.; Sternemann, C.; Paulus, M.; De Feyter, S.; Roeffaers, M.; Debroye, E.; Hofkens, J.; Pradhan, B. Two-Dimensional Perovskites with Alternating Diammonium and Methylammonium Cations in the Interlayer Space for Stable Light-Emitting Diodes. *J. Phys. Chem. Lett.* **2025**, *16* (32), 8353–8362. https://doi.org/10.1021/acs.jpclett.5c01860.
(98) Sun, S.; Huang, P.; Wu, X.; Chen, C.; Hu, X.; Bai, Z.; Pushkarev, A.; Zhong, H. Ligand Exchange-Induced Shape Transformation of CsPbBr3 Nanocrystals Boosts the Efficiency of Perovskite Light-Emitting Diodes. *J. Phys. Chem. C* **2024**, *128* (8), 3602–3608. https://doi.org/10.1021/acs.jpcc.4c00155.

ASSOCIATED CONTENT

Supporting Information. Experimental Section, UV-PL, PLQY, Additional STEM images, elemental mapping, indexing of GIWAXS 1D linecut patterns, XPS, ^{1}H-NMR, SAXS, power law exponent of fractal dimension, picosecond fluorescence decay traces and decay components, wide-field PL images and representative PL blinking trajectories, cross-sectional SEM image of LED, performance matrices of LEDs.

The following PDF file is available free of charge.

AUTHOR INFORMATION

Corresponding Author

*Bapi Pradhan. *Eduard Fron. *Johan Hofkens.

Department of Chemistry, KU Leuven, Celestijnenlaan 200F, 3001 Heverlee (Belgium)

E-mail: bapi.pradhan@kuleuven.be, eduard.fron@kuleuven.be, johan.hofkens@kuleuven.be

Author Contributions

B.P. conceived the science and performed most of the experiments, analysis, coordinated the research, and wrote the manuscript with the input from all the authors under the supervision of J.H. I.S. performed the STEM imaging and analysis under the supervision of S.B. S.K., P.W., H.A., B.P. performed the transmissions SAXS experiments. S.K. & B.P processed and analyzed the transmission SAXS data under the supervision of H.A. A.M. performed the PL blinking measurements and analysis under the supervision of E.D. A.V. performed the LED device fabrication and characterizations under the supervision of I.M.S & A.F.G. J.V. & P.W performed the steady state spectroscopy and DLS measurement under the supervision of J.H. & B.P. J.R & I.U. performed the XPS measurement and analysis under the supervision of A.F.G. T.J.N.H. performed the NMR spectroscopy under the supervision of D.S. M.P & C.S analyzed

the WAXS, GIWAXS and GISAXS analysis. E.F. measured and analyzed time-resolved spectroscopy data. All the author revised the manuscript. The manuscript was written through contributions of all authors. All authors have given approval to the final version of the manuscript. ‡These authors contributed equally.

Funding Sources

Any funds used to support the research of the manuscript should be placed here (per journal style).

ACKNOWLEDGMENT

The authors acknowledge financial support from the Research Foundation - Flanders (FWO Grant Numbers S002019N and G098319N), the Research Foundation - Flanders through a postdoctoral fellowship to B.P. (FWO Grant Numbers 1275521N) and doctoral fellowship to I.S. (SB-FWO project 1SHA024N) and the KU Leuven Research Fund (STG/21/010, C14/19/079 and iBOF-21-085). B. P. acknowledges Industrieel Onderzoeksfonds KU Leuven (IOF)-VTI-25-00160. Within the framework of the NFFA-Europe (Transnational Access Activity, ID446), this project received funding from the EU-H2020 Research and Innovation Programme under grant agreement no. 654360 for access to the CERIC-ERIC's Austrian SAXS beamline provided by Graz University of Technology at Elettra-Sincrotrone Trieste, Italy. T.J.N.H. thanks the Research Foundation-Flanders (Fonds voor Weten-schappelijk Onderzoek-Vlaanderen) for its support via a senior post-doctoral fellowship (1253824N). D.S. thanks the KU Leuven grant (STG-18-00289) and Research Foundation - Flanders (Fonds voor Weten-schappelijk Onderzoek - Vlaanderen) PorMedNMR grant (G0D5419N). The authors thank Prof. J.-P. Locquet and Dr. K. Schouteden (Department of Physics and Astronomy, KU Leuven) for the use of their laboratory's DLS and zeta potential setups. J.V. thanks the Research Foundation-Flanders (FWO) for FWO-FR fellowship 11F3520N. A.F.G.-R. thanks to ANID for the financial support through the FONDECYT

Iniciación Project (Grant n°11240161) and Vinculación Internacional Project (FOVI240255). J.R.-P. thanks the Ministry of Education, Youth and Sports of the Czech Republic for the support of large research infrastructures CEMNAT (project LM2023037). This work has been partially funded by the Generalitat Valenciana via Prometeo Grant Q-Solutions (CIPROM/2021/078) and the project PLEDs (PID2022-140090 OB-C21), funded by the MCIN/AEI/10.13039/501100011033/FEDER, UE.

ABBREVIATIONS

NCs Nanocrystals, PL Photoluminescence, SAXS Small angle X-ray scattering, WAXS Wide angle X-ray scattering, GIWAXS Grazing incident wide angle X-ray scattering, GISAXS Grazing incident small angle X-ray scattering, STEM Scanning transmission electron microscopy, XPS X-ray photoelectron spectroscopy, LEDs light emitting diode.

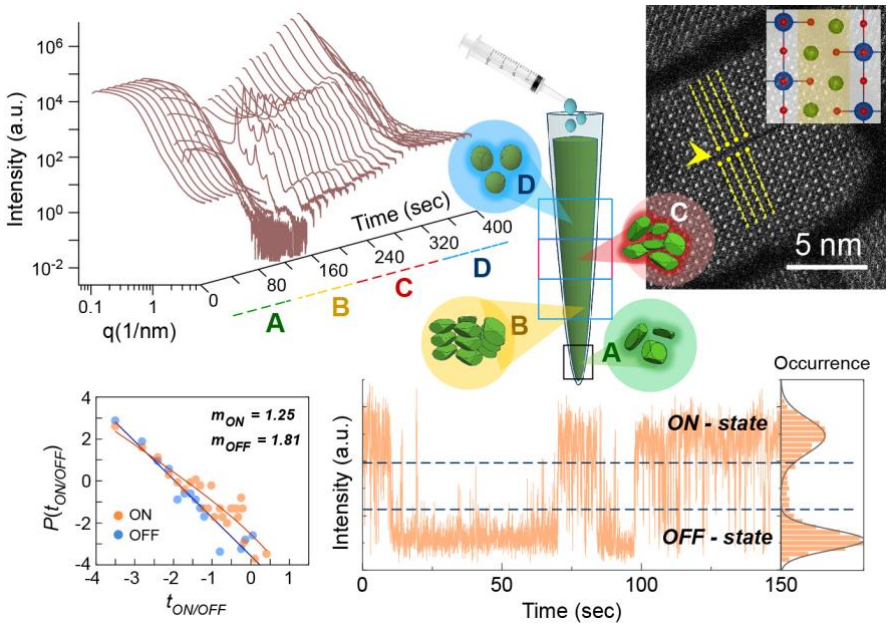


Table of Contents